J. Mech. Phys. Solids 207 (2026) 106426

Contents lists available at ScienceDirect

Journal of the Mechanics and Physics of Solids

journal homepage: www.elsevier.com/locate/jmps

A neural-network-enhanced micromechanical framework with evolving reference medium for nonlinear heterogeneous materials

Ce Chen [a], Liujun Wu [a], Chenyang Xin [a], Wenbin Liu [b], Xin Yi [a,c], Huiling Duan [a,c,*]

[a] School of Mechanics and Engineering Science, Peking University, Beijing 100871, China
[b] Department of Mechanical Engineering, City University of Hong Kong, Hong Kong, China
[c] State Key Laboratory for Turbulence and Complex Systems, HEDPS, CAPT and IFSA, Collaborative Innovation Center of MoE, Peking University, Beijing 100871, China

ARTICLE INFO

Keywords:
Nonlinear micromechanics
Homogenization
Reference medium
Physics-guided neural networks

ABSTRACT

The mechanical response of nonlinear heterogeneous materials is strongly influenced by the deformation-dependent spatial variation of properties in the matrix and inclusions. Conventional micromechanical approaches, typically based on linearization techniques and uniform moduli within each material phase, often fail to capture the effective response of such nonlinear systems, where the local tangent modulus acts as a deformation-dependent measure of stiffness rather than an intrinsic material property. Here, we present a neural-network-enhanced micromechanical framework built upon an evolving nonlinear reference medium with spatially non-uniform tangent moduli, for composites comprising an isotropic matrix and isotropic spherical inclusions with nonlinear interfacial effects. Building on a single-inclusion configuration, where an inclusion is embedded in a reference medium, we introduce two physics-guided neural networks that capture the spatial variation with local deformation states. One network models the inclusions with prescribed properties, while the other represents the reference medium, whose material properties evolve with macroscopic deformations. By enforcing the interfacial displacement–traction condition, we identify the varying properties of the reference medium and determine the effective tangent modulus of the composite. Applied to nonlinear particle-reinforced elastomers at high volume fractions, the framework significantly outperforms classical micromechanical approaches. Moreover, the trained model demonstrates remarkable generalization across diverse nonlinear behaviors of inclusions and matrix, interfacial conditions, loading modes, and volume fractions—without retraining. The framework also extends naturally to plasticity problems, yielding accurate predictions for porous plastic solids. This work establishes a new pathway for integrating neural networks into the derivation of micromechanical relations for complex nonlinear composites.

1. Introduction

The accurate prediction of effective properties in heterogeneous materials—particularly in nonlinear regimes—is essential for the design, characterization, and optimization of a wide range of composite systems, including biomedical materials, rubber composites, and solid propellants (Wang et al., 2023; Shi et al., 2024). Building on the foundational work of equivalent inclusion theory (Eshelby, 1957), micromechanical methods have been extensively developed and applied to estimate the macroscopic response of composites

* Corresponding author at: School of Mechanics and Engineering Science, Peking University, Beijing 100871, China.
E-mail address: hlduan@pku.edu.cn (H. Duan).

https://doi.org/10.1016/j.jmps.2025.106426
Received 7 September 2025; Received in revised form 9 November 2025; Accepted 15 November 2025
Available online 15 November 2025

under linear conditions (Rao et al., 2000; Duan et al., 2006). Classical approaches such as the dilute approximation, Mori–Tanaka (MT) method, and self-consistent (SC) method remain widely used for linear problems (Eshelby, 1957; Mori and Tanaka, 1973; Hill, 1965), and have been progressively extended to incorporate interfacial effects at the inclusion–matrix interface (Dingreville et al., 2005; Firooz et al., 2019; Heitbreder et al., 2021).

However, when large deformations or strong nonlinearities are involved, due to geometric effects, material behavior, or damage at interfaces, traditional micromechanical theories often become inadequate. Interfaces may exhibit softening or decohesion, and the surrounding matrix may undergo non-uniform deformations (Inglis et al., 2007; Spring and Paulino, 2015; Spannraft et al., 2023). The complexities arising from concurrent nonlinearities in constituents and interfaces, challenge the assumptions of uniform field distributions inherent in classical models.

To improve micromechanical modeling under such conditions, various strategies have been proposed to refine the role of the reference medium surrounding inclusions. The three-phase and generalized self-consistent models introduced by Christensen and Lo (1979), Christensen (1990) and further extended in the multiply coated inclusion-reinforced framework (Hervé and Zaoui, 1995) offer enhanced representations of the inclusion environment. These models have been modified to incorporate interfacial effects (Duan et al., 2005; Hervé-Luanco, 2020). In nonlinear problems, the response of the reference medium is typically updated through stepwise discretization and linearization procedures from variational approaches (Ponte Castañeda, 2002; Avazmohammadi and Ponte Castañeda, 2013). For instance, discrete schemes have been proposed to solve viscoelastic–plastic problems by updating the tangent modulus of the reference medium iteratively using the SC method (Sabar et al., 2002; Xiao et al., 2015).

Nonetheless, a critical limitation of these methods lies in their reliance on linearly derived reference media and uniform field approximations, which are only valid under infinitesimal strains. The resulting models struggle to account for heterogeneous modulus distributions, evolving non-uniform deformations, and interfacial nonlinearities in finite deformation regimes (Chen et al., 2024; Brassart et al., 2009). Therefore, how micromechanical frameworks can robustly address the coexistence of matrix, inclusion, and interfacial nonlinearities remains a major challenge.

Recent advances in machine learning (ML) have opened promising avenues for addressing such complex nonlinear problems. Broadly, existing work in ML-assisted homogenization follows two main directions. The first focuses on data-driven methods that enhance or replace traditional micromechanical or multiscale procedures, where neural networks are trained directly on multiscale simulation data (Le et al., 2015; Gholami et al., 2023). With a surrogate model for nonlinear constitutive laws, Lu et al. (2021) proposed a hybrid neural-network-interpolation approach within multilevel finite-element (FE^2) methods, enabling accurate solutions to random nonlinear multiscale problems even with limited data. Similarly, to handle materials with internal variables and history-dependent properties, Logarzo et al. (2021) incorporated microstructurally-informed, machine-learning-based constitutive models into conventional finite element solver in concurrent multiscale models. Taking a different strategy, Benaimeche et al. (2022) developed a k-means FE^2 scheme that groups Gauss points with deformation states into clusters, providing computational acceleration for similar history-dependent systems without relying on surrogate constitutive models.

The second branch emphasizes embedding known physical constraints to reduce the demand for large training datasets. Physics-informed neural networks (PINNs) incorporate governing equations directly into the loss function (Raissi et al., 2019; Wu et al., 2023). Building on this idea, physics-guided neural networks (PGNNs) explicitly encode constitutive structure or invariance principles into the network architecture itself. Notable developments include the incorporation of rotational invariance via Gaussian processes (Frankel et al., 2020), the embedding of deformation invariants and structural tensors (Linka et al., 2021), and the establishment of invariant relations within an infinite isotropic reference medium (Chen et al., 2024). Beyond homogenization, ML approaches have also shown promise in accelerating computationally intensive tasks, such as large-scale topology optimization using problem-independent learning strategies (Huang et al., 2022), as well as identifying the dominant microstructural mechanisms in fracture nucleation of complex alloys (Hasan et al., 2023).

In this work, we propose a nonlinear micromechanical framework that integrates two PGNNs with the micromechanical theory. Using a single-inclusion scheme, one PGNN captures the nonlinear response of the isotropic inclusion with prescribed properties, while another determines the evolving, spatially- and deformation-dependent tangent modulus of the isotropic reference medium. By enforcing the interfacial displacement–traction condition, the framework identifies the evolving properties of the reference medium and corresponding concentration tensors, and efficiently computes the effective tangent modulus under large deformations. Applied to composites with nonlinear matrix, inclusions, and interfaces, the framework outperforms traditional approaches and generalizes across loading modes, volume fractions, and material properties, extending naturally to plasticity and porous solids.

While our previous work (Chen et al., 2024) established a neural-network-assisted micromechanical scheme, the current study introduces several key advances that significantly extends its theoretical foundation and computational versatility. First, we reformulate the original total-form expression into a rigorous incremental framework, reducing computational complexity and enabling real-time stress–strain evolution. Second, by constructing the inclusion nonlinear response that captures its non-uniform tangent modulus via a tailored neural network, the method transcends the rigid-inclusion constraint and generalizes to arbitrary nonlinear isotropic inclusions—a capability that was previously unattainable. Third, we introduce an adaptive reference medium whose properties evolve dynamically via optimization under modulus-consistency constraint. This innovation eliminates retraining when analyzing composites with varying matrix behaviors, addressing a critical bottleneck in our prior model and many existing neural-network-based schemes. Collectively, these advances not only improve numerical performance and robustness but also establish a unifying, model-agnostic framework for a broad class of nonlinear micromechanical problems with minimal manual intervention.

The remainder of this paper is organized as follows. Section 2 presents the theoretical foundation of the proposed framework, including invariant relations for the isotropic reference medium and inclusions and the derivation of the effective tangent modulus.

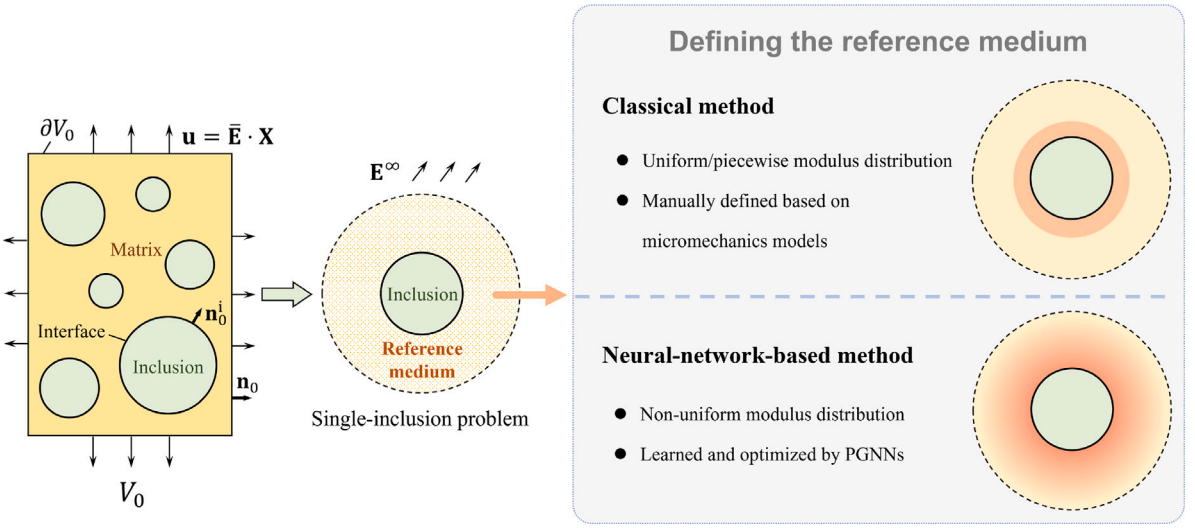

Fig. 1. Schematic overview of the nonlinear micromechanical framework. $\bar{\mathbf{E}}$ denotes the prescribed macroscopic engineering strain applied to the composite boundary. Following a standard micromechanical procedure, the original multi-inclusion homogenization problem is reduced to a single-inclusion problem, where a far-field strain $\mathbf{E}^\infty$ is applied to the reference medium. A comparison is shown between classical and neural-network-based strategies for defining the reference medium.

Section 3 details the neural network architecture and training process. Section 4 provides numerical validations under various nonlinear conditions and assesses the generalization capability of the framework. Section 5 applies this framework to porous plastic solids. Conclusions are summarized in Section 6.

Throughout the manuscript, the notation "$\dot{\bullet}$" denotes the derivative of a physical quantity with respect to time or the deformation process. The symbol "$\{\bullet\}$" indicates the set of dimensionless quantities, and "$\bar{\bullet}$" represents volume-averaged quantities. The superscripts "i", "m", "int", "rm", and "h" represent inclusion, matrix, interface, reference medium, and macroscopic homogenized material, respectively.

2. Theoretical framework

This section introduces the theoretical foundation of the proposed micromechanical scheme, including the homogenization formulation, the construction of an evolving isotropic reference medium, and the use of PGNNs for inferring the effective tangent modulus.

2.1. Nonlinear micromechanical scheme

We consider a heterogeneous medium, consisting of a matrix and multiple embedded inclusions, occupying a domain V_0 with boundary ∂V_0 in the reference configuration $\mathscr{B}_0$ (Fig. 1). Both the inclusions and the matrix are taken as isotropic and homogeneous. Material points are denoted by their spatial coordinates $\mathbf{X}$ in $\mathscr{B}_0$ and by $\mathbf{x}$ in the current configuration $\mathscr{B}$. The deformation gradient is defined as $\mathbf{F} = \partial \mathbf{x}/\partial \mathbf{X}$.

As a representative case, we focus on the homogenization problem under an average strain boundary condition. The system satisfies the equilibrium and kinematic conditions:

$$\begin{cases} \mathbf{S} \cdot \nabla_0 = 0, \quad \text{in} \quad V_0 = V_0^{\mathrm{i}} + V_0^{\mathrm{m}}, & \text{(1a)} \\ \mathbf{u} = \bar{\mathbf{E}} \cdot \mathbf{X}, \quad \text{at} \quad \partial V_0, & \text{(1b)} \end{cases}$$

where $\mathbf{S}$ is the first Piola–Kirchhoff stress, ∇_0 denotes the divergence operator in the reference configuration $\mathscr{B}_0$, $\mathbf{u}$ is the prescribed boundary displacement (excluding rigid-body rotation), and $\bar{\mathbf{E}}$ is the corresponding macroscopic engineering strain. The average deformation gradient is represented as $\bar{\mathbf{F}} = \frac{1}{V_0}\int_{V_0} \mathbf{F} \mathrm{d}V_0 = \frac{1}{V_0}\int_{\partial V_0} (\mathbf{u} + \mathbf{X})\mathbf{n}_0 \mathrm{d}A_0 = \bar{\mathbf{E}} + \mathbf{I}$, where $\mathrm{d}V_0$, and $\mathrm{d}A_0$ represent infinitesimal volume and area elements in the reference configuration $\mathscr{B}_0$ and $\mathbf{I}$ is the identity tensor. $\mathbf{n}_0$ is the outward normal direction of the boundaries in $\mathscr{B}_0$. The goal of homogenization is to establish the macroscopic constitutive relation between $\bar{\mathbf{E}}$ and the volume-averaged stress $\bar{\mathbf{S}} = \frac{1}{V_0}\int_{V_0} \mathbf{S} \mathrm{d}V_0 = \frac{1}{V_0}\int_{\partial V_0} \mathbf{t}\mathbf{X} \mathrm{d}A_0$. In this work, the traction $\mathbf{t}$ is $\mathbf{t} = \mathbf{S} \cdot \mathbf{n}_0$, which represents the force in the current configuration $\mathscr{B}$ per area in reference configuration $\mathscr{B}_0$.

The local constitutive relation between stress $\mathbf{S}$ and deformation gradient $\mathbf{F}$ is

$$\mathbf{S} = \mu_{\mathrm{ref}} \Psi(c, \mathbf{F}), \tag{2}$$

where μ_{ref} denotes a prescribed reference modulus, which may be chosen uniformly across different materials (e.g., the shear modulus of the matrix). Here, Ψ is a known constitutive mapping and c is a set of intrinsic, dimensionless material parameters that vary with the constituent (e.g., Ψ^{m} and c^{m} for the matrix). In general, Ψ and c span a class of admissible constitutive behaviors. For example, in the Mooney–Rivlin model (Rivlin and Saunders, 1951), a hyperelastic constitutive law for rubber-like materials, c could be the coefficient of the material's strain energy normalized by μ_{ref}.

The macroscopic stress–strain relation for the homogenized composite is taken in an analogous mapping form Ψ^{h}

$$\bar{\mathbf{S}} = \mu_{\text{ref}} \Psi^{\text{h}}(c^{\text{h}}, \bar{\mathbf{E}} + \mathbf{I}), \tag{3}$$

where, unlike in actual constituent materials, the parameter $c^{\text{h}}(\bar{\mathbf{E}})$ evolves with the macroscopic strain $\bar{\mathbf{E}}$.

Following Hill (1972), the volume-averaged strain and stress of the heterogeneous material can be written as

$$\begin{cases} \bar{\mathbf{E}} = v^{\text{m}} \bar{\mathbf{E}}^{\text{m}} + \sum_k v_k^{\text{i}} (\bar{\mathbf{E}}_k^{\text{i}} + \bar{\mathbf{E}}_k^{\text{int}}), & \text{(4a)} \\ \bar{\mathbf{S}} = v^{\text{m}} \bar{\mathbf{S}}^{\text{m}} + \sum_k v_k^{\text{i}} (\bar{\mathbf{S}}_k^{\text{i}} + \bar{\mathbf{S}}_k^{\text{int}}), & \text{(4b)} \end{cases}$$

where k indexes the inclusions, v^{m} and v_k^{i} denote the initial volume fractions of the matrix and the kth inclusion, respectively. In the following, the subscript k is omitted for clarity when referring to general inclusion quantities. Here, $\bar{\mathbf{E}}^{\text{i}}$ and $\bar{\mathbf{E}}^{\text{m}}$ are the volume averages of $\mathbf{F}^{\text{i}} - \mathbf{I}$ and $\mathbf{F}^{\text{m}} - \mathbf{I}$, respectively, expressed as $\bar{\mathbf{E}}^{\text{i}} = \frac{1}{V_0^{\text{i}}} \int_{V_0^{\text{i}}} (\mathbf{F}^{\text{i}} - \mathbf{I}) \mathrm{d}V_0$ and $\bar{\mathbf{E}}^{\text{m}} = \frac{1}{V_0^{\text{m}}} \int_{V_0^{\text{m}}} (\mathbf{F}^{\text{m}} - \mathbf{I}) \mathrm{d}V_0$. Similarly, the average stress $\bar{\mathbf{S}}^{\text{i}}$ and $\bar{\mathbf{S}}^{\text{m}}$ are defined as $\bar{\mathbf{S}}^{\text{i}} = \frac{1}{V_0^{\text{i}}} \int_{V_0^{\text{i}}} \mathbf{S}^{\text{i}} \mathrm{d}V_0$ and $\bar{\mathbf{S}}^{\text{m}} = \frac{1}{V_0^{\text{m}}} \int_{V_0^{\text{m}}} \mathbf{S}^{\text{m}} \mathrm{d}V_0$. $\bar{\mathbf{E}}^{\text{int}}$ and $\bar{\mathbf{S}}^{\text{int}}$ are quantities associated with the interfacial strain and stress, respectively, as defined later.

By applying the divergence theorem, $\bar{\mathbf{E}}^{\text{i}}$ and $\bar{\mathbf{S}}^{\text{i}}$ within each inclusion can be expressed via surface integrals of the displacement $\mathbf{u}^{\text{i}}$ and traction $\mathbf{t}^{\text{i}}$ over the inclusion boundary ∂V_0^{i}, expressed as $\bar{\mathbf{E}}^{\text{i}} = \frac{1}{V_0^{\text{i}}} \int_{\partial V_0^{\text{i}}} \mathbf{u}^{\text{i}} \mathbf{n}_0^{\text{i}} \mathrm{d}A_0$, and $\bar{\mathbf{S}}^{\text{i}} = \frac{1}{V_0^{\text{i}}} \int_{\partial V_0^{\text{i}}} \mathbf{t}^{\text{i}} \mathbf{X} \mathrm{d}A_0$, where $\mathbf{n}_0^{\text{i}}$ denotes the outward normal direction of the inclusion surface in the reference configuration $\mathscr{B}_0$.

Note that, in general, $\bar{\mathbf{E}}^{\text{i}}$ and $\bar{\mathbf{E}}^{\text{m}}$ in Eq. (4) are not necessarily symmetric and differ from the engineering strain. In the present work, however, we assume that the isotropic inclusions are spherical and distributed isotropically. This geometric uniformity of the inclusions ensures that each inclusion deforms with consistent symmetry and without rotation under the prescribed displacement $\mathbf{u}$ or the corresponding macroscopic strain $\bar{\mathbf{E}}$ in Eq. (1) (Chen et al., 2024), yielding $\bar{\mathbf{E}}^{\text{i}} = (\bar{\mathbf{E}}^{\text{i}})^{\text{T}}$ and $\bar{\mathbf{E}}^{\text{m}} = (\bar{\mathbf{E}}^{\text{m}})^{\text{T}}$. Consequently, $\bar{\mathbf{E}}^{\text{i}}$ and $\bar{\mathbf{E}}^{\text{m}}$ coincide with the engineering strain corresponding to the volume averages of $\mathbf{F}^{\text{i}}$ and $\mathbf{F}^{\text{m}}$. The average strain and stress of the isotropic matrix are then approximated to obey the same relationship as Eq. (2), namely $\bar{\mathbf{S}}^{\text{m}} = \mu_{\text{ref}} \Psi^{\text{m}}(c^{\text{m}}, \bar{\mathbf{E}}^{\text{m}} + \mathbf{I})$. This assumption is exact in linear elasticity and valid within the scope of first-order homogenization methods (Govindjee and Simo, 1991).

In the presence of interfacial discontinuities, additional contributions arise from the possible displacement jump $\Delta\mathbf{u} = \mathbf{u}^{\text{m}} - \mathbf{u}^{\text{i}}$ and the traction jump $\Delta\mathbf{t} = (\mathbf{S}^{\text{m}} - \mathbf{S}^{\text{i}}) \cdot \mathbf{n}_0^{\text{i}}$ across the inclusion–matrix interface. The interface model enforces the relations between the displacement $\mathbf{u}^{\text{i}}$ and stress $\mathbf{S}^{\text{i}}$ on the inclusion side and the displacement $\mathbf{u}^{\text{m}}$ and stress $\mathbf{S}^{\text{m}}$ on the matrix side. The displacement and stress jump leads to interfacial strain and stress terms given by $\bar{\mathbf{E}}^{\text{int}} = \frac{1}{V_0^{\text{i}}} \int_{\partial V_0^{\text{i}}} \frac{1}{2} (\Delta\mathbf{u}\mathbf{n}_0^{\text{i}} + \mathbf{n}_0^{\text{i}} \Delta\mathbf{u}) \mathrm{d}A_0$ and $\bar{\mathbf{S}}^{\text{int}} = \frac{1}{V_0^{\text{i}}} \int_{\partial V_0^{\text{i}}} \Delta\mathbf{t}\mathbf{X} \mathrm{d}A_0$, following the treatment of Benveniste and Miloh (2001) and Tan et al. (2005).

To solve this nonlinear homogenization problem, we analyze the evolution of stress and strain in each inclusion, denoted as $\dot{\bar{\mathbf{E}}}^{\text{i}}$ and $\dot{\bar{\mathbf{S}}}^{\text{i}}$, respectively. These represent derivatives with respect to the macroscopic deformation process. For example, if the macroscopic uniaxial tensile strain ε is used to characterize the loading path, then $\dot{\bar{\mathbf{E}}}^{\text{i}} = \partial \bar{\mathbf{E}}^{\text{i}} / \partial \varepsilon$ and $\dot{\bar{\mathbf{S}}}^{\text{i}} = \partial \bar{\mathbf{S}}^{\text{i}} / \partial \varepsilon$. Via linear mapping relations, characterized by the strain and stress concentration tensors $\mathbf{R}^{\text{c}}$ and $\mathbf{U}^{\text{c}}$, the evolution of the macroscopic strain $\dot{\bar{\mathbf{E}}} = \partial \bar{\mathbf{E}} / \partial \varepsilon$ and stress $\dot{\bar{\mathbf{S}}} = \partial \bar{\mathbf{S}} / \partial \varepsilon$ are, respectively, given as

$$\dot{\bar{\mathbf{E}}}^{\text{i}} = \mathbf{R}^{\text{c}} : \dot{\bar{\mathbf{E}}} \quad \text{and} \quad \dot{\bar{\mathbf{S}}}^{\text{i}} = \mathbf{U}^{\text{c}} : \dot{\bar{\mathbf{S}}}. \tag{5}$$

For conciseness, we adopt the strain-based form involving $\bar{\mathbf{E}}$ and $\mathbf{R}^{\text{c}}$ throughout the remainder of this work.

When interfacial displacement discontinuities are present, their contribution to the strain rate is captured by an interfacial strain concentration tensor $\mathbf{W}^{\text{c}}$, such that

$$\dot{\bar{\mathbf{E}}}^{\text{int}} = \mathbf{W}^{\text{c}} : \dot{\bar{\mathbf{E}}}. \tag{6}$$

The tangent modulus tensor of the overall composite is defined by $\mathbf{L}^{\text{h}} = \mathrm{d}\bar{\mathbf{S}} / \mathrm{d}\bar{\mathbf{E}}$. According to Duan et al. (2005), the effective tangent modulus tensor can be calculated from Eqs. (4)–(6) as

$$\mathbf{L}^{\text{h}} = \bar{\mathbf{L}}^{\text{m}} + \sum_k v_k^{\text{i}} [(\bar{\mathbf{L}}_k^{\text{i}} - \bar{\mathbf{L}}^{\text{m}}) : \mathbf{R}_k^{\text{c}} - \bar{\mathbf{L}}^{\text{m}} : \mathbf{W}_k^{\text{c}}], \tag{7}$$

where $\bar{\mathbf{L}}^{\text{m}} = \mathrm{d}\bar{\mathbf{S}}^{\text{m}} / \mathrm{d}\bar{\mathbf{E}}^{\text{m}}$ and $\bar{\mathbf{L}}^{\text{i}} = \mathrm{d}\bar{\mathbf{S}}^{\text{i}} / \mathrm{d}\bar{\mathbf{E}}^{\text{i}}$.

If the interface stress model is adopted, Eq. (6) is replaced by $\dot{\bar{\mathbf{S}}}^{\text{int}} = \bar{\mathbf{L}}^{\text{m}} : \mathbf{T}^{\text{c}} : \dot{\bar{\mathbf{E}}}$ with $\mathbf{T}^{\text{c}}$ as another interfacial strain concentration tensor. Accordingly, the term $-\bar{\mathbf{L}}^{\text{m}} : \mathbf{W}_k^{\text{c}}$ in Eq. (7) is replaced by $\bar{\mathbf{L}}^{\text{m}} : \mathbf{T}_k^{\text{c}}$.

So far, the central challenge in the nonlinear homogenization problem defined by Eq. (1) lies in the accurate estimation of the concentration tensors. In general, analytical solutions for these tensors are intractable in systems containing multiple isotropic inclusions and imperfect interfaces. Consequently, micromechanical schemes commonly reduce the problem to a simplified single-inclusion problem (SIP) (Fig. 1), from which approximate concentration tensors can be extracted. In the following section, we present an explicit solution to these concentration tensors by solving a nonlinear SIP.

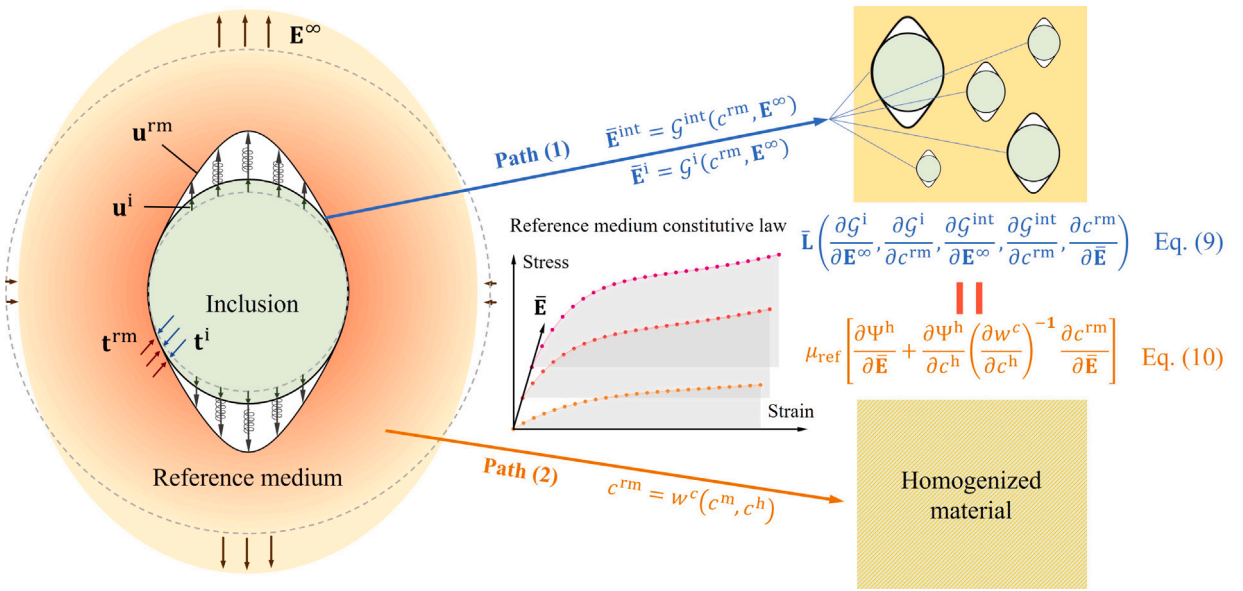

Fig. 2. Schematic representation of the nonlinear SIP. The far-field strain $\mathbf{E}^\infty$ applied to the reference medium induces system deformation. Solving the SIP yields the average strain for each isotropic spherical inclusion and the contribution from its interface. The isotropic reference medium is constructed to reflect both matrix properties and macroscopic homogenized behavior. The constitutive law of the reference medium, governed by the parameter $c^{rm}(\bar{\mathbf{E}})$, evolves with the macroscopic strain $\bar{\mathbf{E}}$. A comparison between tangent modulus tensors obtained through two distinct pathways enables the determination of the parameter variation in the reference medium. For an isotropic reference medium and interface, an axisymmetric far-field strain $\mathbf{E}^\infty$ in the SIP formulation results in an axisymmetric mechanical response.

2.2. Evolving reference medium in the nonlinear single-inclusion problem (SIP)

2.2.1. Reference medium with non-uniformly distributed modulus

In the SIP illustrated in Fig. 2, a spherical inclusion is embedded in an infinite isotropic reference medium. The isotropic inclusion and the interface possess the same properties as in the homogenization problem (Eqs. (1)–(5)). At the interface, the matrix displacement and stress are replaced by those of the reference medium, denoted as $\mathbf{u}^{rm}$ and $\mathbf{S}^{rm}$. Thus across the inclusion-reference medium interface, the displacement jump is denoted by $\Delta\mathbf{u} = \mathbf{u}^{rm} - \mathbf{u}^i$ and the traction jump is $\Delta\mathbf{t} = (\mathbf{S}^{rm} - \mathbf{S}^i)\cdot\mathbf{n}_0^i$. The reference medium is conceptualized to emulate the realistic mechanical environment experienced by the inclusion. Traditionally, it has been modeled with a simple modulus distribution, uniform or piecewise uniform, based on classical micromechanical approximations such as the Mori–Tanaka or generalized self-consistent schemes (Mori and Tanaka, 1973; Christensen and Lo, 1979). However, when modeling the mechanical behavior of nonlinear heterogeneous materials under finite deformations, the tangent modulus of the reference medium is generally spatially inhomogeneous. This inhomogeneity arises from geometric nonlinearity and non-uniform strain fields, and is typically negligible only in the infinitesimal deformation regime. As a result, classical Eshelby-type solutions, which assume uniform tangent modulus, can lead to substantial inaccuracies under nonlinear conditions.

To overcome this limitation, we construct the SIP using an isotropic reference medium with a spatially varying modulus that evolves with deformation. This inhomogeneous modulus field is generated from the nonlinear response of a homogeneous reference medium governed by a prescribed custom-defined constitutive law in the form of, for example, $\mathbf{S}^{rm} = \mu_{ref}\boldsymbol{\Psi}^{rm}(c^{rm}, \mathbf{F}^{rm})$, where the material parameters $c^{rm}(\bar{\mathbf{E}})$ evolve with the macroscopic strain $\bar{\mathbf{E}}$, while the function form of $\boldsymbol{\Psi}^{rm}$ remains unchanged. In this way, the evolving reference medium effectively approximates the complex, deformation-dependent, and spatially inhomogeneous mechanical environment surrounding the inclusion, thereby enhancing the fidelity of the nonlinear homogenization model in micromechanics. Note that the inclusion properties c^i are typically assumed to remain fixed during deformation ($\partial c^i/\partial\bar{\mathbf{E}} = \mathbf{0}$).

By solving the SIP under a prescribed far-field strain $\mathbf{E}^\infty$ (an unknown quantity), the average inclusion strain $\bar{\mathbf{E}}^i$ and interfacial strain contribution $\bar{\mathbf{E}}^{int}$ can be obtained. These relationships are represented by nonlinear mappings $\mathcal{G}^i$ and $\mathcal{G}^{int}$ from the far-field input $\mathbf{E}^\infty$ and the reference medium properties c^{rm} to $\bar{\mathbf{E}}^i$ and $\bar{\mathbf{E}}^{int}$, respectively:

$$\bar{\mathbf{E}}^i = \mathcal{G}^i(c^{rm}, \mathbf{E}^\infty) \quad \text{and} \quad \bar{\mathbf{E}}^{int} = \mathcal{G}^{int}(c^{rm}, \mathbf{E}^\infty). \tag{8}$$

The micromechanical model relies on establishing a correspondence between the SIP and both the surrounding matrix and the macroscopic composite, particularly in terms of boundary conditions and material properties. Specifically, $\mathbf{E}^\infty$ and c^{rm} can be described through mapping functions $w^{\mathbf{E}}$ and w^c as

$$\begin{cases} \mathbf{E}^\infty = w^{\mathbf{E}}(\bar{\mathbf{E}}^m, \bar{\mathbf{E}}), & \text{(9a)} \\ c^{rm} = w^c(c^m, c^h). & \text{(9b)} \end{cases}$$

The inclusion–inclusion interaction and the inclusion–matrix interaction are reflected in the specific choice of Eq. (9). Concrete expressions of these mappings for particular models are provided in Section 4.1.

By combining Eqs. (4)–(9), the concentration tensors $\mathbf{R}^{\mathrm{c}}$ and $\mathbf{W}^{\mathrm{c}}$ can be derived from the nonlinear mappings $\mathcal{G}^{\mathrm{i}}$ and $\mathcal{G}^{\mathrm{int}}$ as shown in Eqs. (A.4). However, in Eqs. (A.4), the evolution of the reference medium properties, represented by $\partial c^{\mathrm{rm}}/\partial\bar{\mathbf{E}}$ (or equivalently $\partial c^{\mathrm{h}}/\partial\bar{\mathbf{E}}$), remains unknown at this stage. Since different choices of c^{rm} result in distinct predictions of the tangent modulus, we introduce a tangent-modulus matching criterion within the nonlinear micromechanical framework. This criterion is employed to identify a self-consistent evolution of the reference medium properties that aligns with the macroscopic mechanical response.

2.2.2. Reference medium property variation via a modulus equivalence rule

The modulus of the reference medium is not only spatially inhomogeneous but also evolves dynamically throughout the deformation process. The evolution of reference medium properties $\partial c^{\mathrm{rm}}/\partial\bar{\mathbf{E}}$ directly influences the macroscopic tangent modulus $\mathbf{L}^{\mathrm{h}} = \mathrm{d}\bar{\mathbf{S}}/\mathrm{d}\bar{\mathbf{E}}$ through Eqs. (4) and (A.4). This leads to an expression of the following form

$$\mathbf{L}^{\mathrm{h}} = \mathbf{L}^{\mathrm{h}}\left(\frac{\partial\mathcal{G}^{\mathrm{i}}}{\partial\mathbf{E}^{\infty}}, \frac{\partial\mathcal{G}^{\mathrm{i}}}{\partial c^{\mathrm{rm}}}, \frac{\partial\mathcal{G}^{\mathrm{int}}}{\partial\mathbf{E}^{\infty}}, \frac{\partial\mathcal{G}^{\mathrm{int}}}{\partial c^{\mathrm{rm}}}, \frac{\partial c^{\mathrm{rm}}}{\partial\bar{\mathbf{E}}}\right). \tag{10}$$

On the other hand, the tangent modulus also can be obtained from the constitutive relation, yielding

$$\mathbf{L}^{\mathrm{h}} = \mu_{\mathrm{ref}}\left[\frac{\partial\Psi^{\mathrm{h}}}{\partial\bar{\mathbf{E}}} + \frac{\partial\Psi^{\mathrm{h}}}{\partial c^{\mathrm{h}}}\left(\frac{\partial w^{c}}{\partial c^{\mathrm{h}}}\right)^{-1}\frac{\partial c^{\mathrm{rm}}}{\partial\bar{\mathbf{E}}}\right]. \tag{11}$$

The derivation of Eq. (11) exploits the fact that c^{m}, the material properties of the isotropic matrix is invariant throughout the deformation. Eqs. (10) and (11) indicate that the macroscopic modulus is influenced by two key factors: the direct effect of the strain $\bar{\mathbf{E}}$, and the indirect effect through changes in the material properties. As shown in Fig. 2, we determine the evolution of c^{rm} with deformation (i.e., $\partial c^{\mathrm{rm}}/\partial\bar{\mathbf{E}}$) by minimizing the discrepancy between the two tangent modulus formulations given in Eqs. (10) and (11). Once the derivatives of the nonlinear mappings $\mathcal{G}^{\mathrm{i}}$ and $\mathcal{G}^{\mathrm{int}}$ in Eq. (10) are obtained, the evolution of the reference medium properties $\partial c^{\mathrm{rm}}/\partial\bar{\mathbf{E}}$ can be determined. The macroscopic tangent modulus $\mathbf{L}^{\mathrm{h}}$ is then fully defined.

2.3. Modified physics-guided neural networks for the nonlinear SIP

The analytical expressions for the nonlinear mappings $\mathcal{G}^{\mathrm{i}}$ and $\mathcal{G}^{\mathrm{int}}$ are generally unavailable due to the complexity introduced by material and geometric nonlinearities. In our previous work (Chen et al., 2024), we proposed a framework based on PGNNs to approximate a special case of $\mathcal{G}^{\mathrm{int}}$ with fixed c^{rm}. However, that approach does not yield explicit forms and suffers from several limitations (e.g., the influence of deformable inclusions has not been taken into account, and the possible property evolution of the reference medium has been ignored) when applied to more general scenarios. In this section, we introduce essential modifications to enhance the applicability and robustness of PGNNs in the nonlinear SIP context. We then derive the incremental form of the physically invariant relations via the differential of the PGNNs. Finally, an explicit formula for the macroscopic tangent modulus tensor is obtained based on the PGNN differentials.

2.3.1. Mechanical response for evolving reference medium

In the SIP, we introduce a spherical coordinate system centered at the spherical inclusion with radius a (Fig. 3). The spherical coordinates are denoted as (R, Θ, Φ), where R is the radial distance, Θ is the polar angle (measured from the positive x-axis), and Φ is the azimuthal angle in the y–z plane (measured from the positive y-axis toward the z-axis). For consistency of description between the inclusion and the reference medium, on a spherical surface of radius R in both the reference medium and the inclusion, the unit normals $\mathbf{n}_0^{\mathrm{rm}}$ and $\mathbf{n}_0^{\mathrm{i}}$ are taken as radially outward, pointing from the center toward the far field. Thus at the interface, the same unit normal $\mathbf{n}_0^{\mathrm{i}} = \mathbf{n}_0^{\mathrm{rm}}$ is adopted on both sides. For SIPs with favorable convexity, the mechanical response of the reference medium in the region between the far-field and the surface at radius R is uniquely determined by the material properties and boundary conditions. The physical quantities governing this response of the traction $\mathbf{t}^{\mathrm{rm}}(R) = \mathbf{S}^{\mathrm{rm}}(R)\cdot\mathbf{n}_0^{\mathrm{rm}}$, include the isotropic reference medium properties c^{rm} in the constitutive model, and the displacement $\mathbf{u}^{\mathrm{rm}}(R)$ as well as the far-field strain $\mathbf{E}^{\infty}$ (serving as the boundary conditions).

Employing Buckingham's Pi theorem (Buckingham, 1914), there is a mapping between the dimensionless traction $\mathbf{T}^{\mathrm{rm}}(R)$ and dimensionless displacement $\mathbf{U}^{\mathrm{rm}}(R)$ of the reference medium at radius R

$$\mathbf{T}^{\mathrm{rm}}(R) = \mathcal{Q}^{\mathrm{rm}}\left(c^{\mathrm{rm}}, \mathbf{U}^{\mathrm{rm}}(R), \mathbf{E}^{\infty}\right), \quad \text{for } R \geq a, \tag{12}$$

where $\mathbf{T}^{\mathrm{rm}}(R) = \mathbf{t}^{\mathrm{rm}}(R)/\mu_{\mathrm{ref}}$ and $\mathbf{U}^{\mathrm{rm}}(R) = \mathbf{u}^{\mathrm{rm}}(R)/R$. Based on Eq. (12), we train the reference medium-PGNN, which models the mapping $\mathcal{Q}^{\mathrm{rm}}$, by taking the dimensionless quantities c^{rm}, $\mathbf{U}^{\mathrm{rm}}(R)$, and $\mathbf{E}^{\infty}$ as inputs, and $\mathbf{T}^{\mathrm{rm}}(R)$ as the target output. The selection of different c^{rm} enables the PGNN to learn the dependence of the mechanical response not only on geometric and loading conditions but also on the evolving material properties of the reference medium.

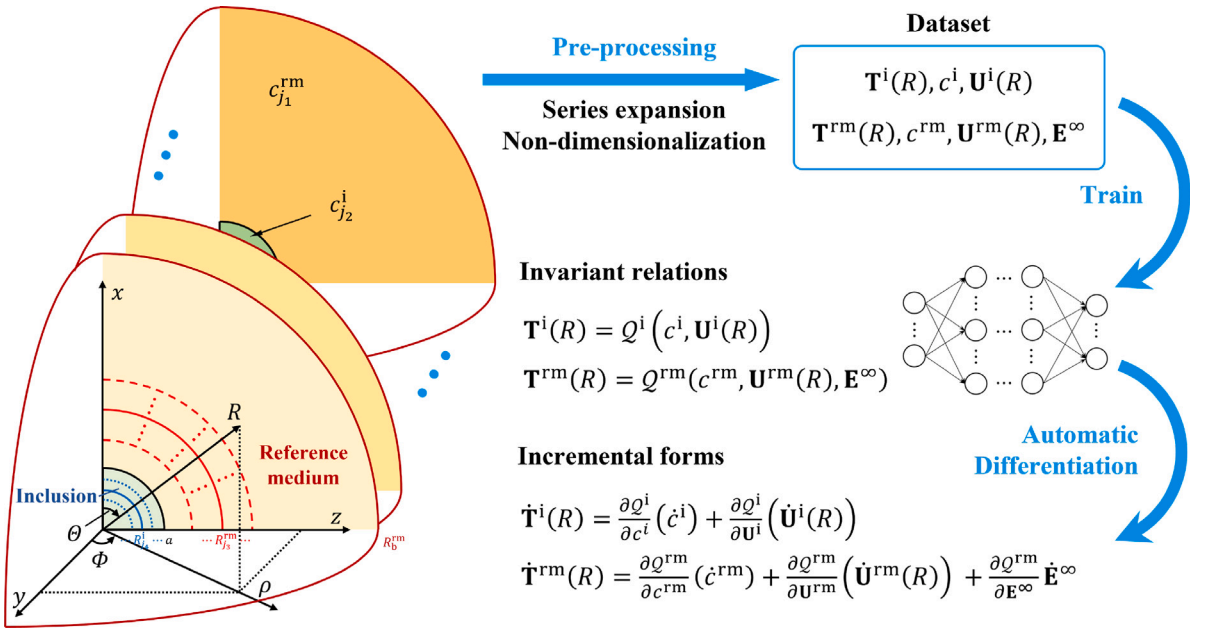

Fig. 3. Schematic of the PGNN framework representing invariant relations in the nonlinear SIP. The network learns dimensionless mappings based on reference medium properties and boundary conditions. Differential forms of the PGNN are subsequently used to evaluate the tangent moduli.

2.3.2. *Neural-network-based mechanical response of the nonlinear inclusion*

Conventional approaches fail to provide solutions to the SIP involving the simultaneous nonlinearities of the isotropic reference medium, inclusion, and interface. Here, we also conduct a dimensional analysis for nonlinear inclusions, focusing on key physical quantities such as traction $\mathbf{t}^{\mathrm{i}}(R) = \mathbf{S}^{\mathrm{i}}(R) \cdot \mathbf{n}_0^{\mathrm{i}}$, displacement $\mathbf{u}^{\mathrm{i}}(R)$, and the associated material parameters.

Following the similar scheme in the previous section for the reference medium, we derive an invariant relationship for the nonlinear isotropic inclusion as

$$\mathbf{T}^{\mathrm{i}}(R) = \mathcal{Q}^{\mathrm{i}}\left(c^{\mathrm{i}}, \mathbf{U}^{\mathrm{i}}(R)\right), \quad \text{for } R \le a, \tag{13}$$

where $\mathbf{T}^{\mathrm{i}}(R) = \mathbf{t}^{\mathrm{i}}(R)/\mu_{\mathrm{ref}}$, c^{i} as the inclusion property, and $\mathbf{U}^{\mathrm{i}}(R) = \mathbf{u}^{\mathrm{i}}(R)/R$. The inclusion-PGNN, which models the mapping $\mathcal{Q}^{\mathrm{i}}$, is trained using the dimensionless quantities c^{i} and $\mathbf{U}^{\mathrm{i}}(R)$ as inputs, and $\mathbf{T}^{\mathrm{i}}(R)$ as the target output.

Both invariant relationships in Eqs. (12) and (13) hold for any radius R. The distributions at varying radii provide distinct input–output pairs for the relationships. This feature facilitates the rapid and large-scale extraction of displacement and traction from mechanical information at any radius R for the neural network (Fig. 3). The network is subsequently used to infer the evolving modulus distribution and to derive a closed form for the effective tangent modulus, which is presented in Section 2.4. Furthermore, the data generation process, detailed in Section 3, can be conducted with high computational efficiency.

In the following derivations, the invariant relations are applied at the inclusion-reference medium interface ($R = a$), and we adopt $\mathbf{T}_a^{\mathrm{rm}} \equiv \mathbf{T}^{\mathrm{rm}}(a)$, $\mathbf{T}_a^{\mathrm{i}} \equiv \mathbf{T}^{\mathrm{i}}(a)$, $\mathbf{U}_a^{\mathrm{rm}} \equiv \mathbf{U}^{\mathrm{rm}}(a)$, and $\mathbf{U}_a^{\mathrm{i}} \equiv \mathbf{U}^{\mathrm{i}}(a)$, denoting the dimensionless traction and displacement distributions on either side of the interface.

For the spherical inclusion, the boundary position vector $\mathbf{X}$ is proportional to $\mathbf{n}_0^{\mathrm{i}}$, such that $\mathbf{X} = a\mathbf{n}_0^{\mathrm{i}}$. This property ensures that the average strains and stresses of both the inclusion and the interface share the same surface–integral representation. Consequently, the strain $\bar{\mathbf{E}}^{\mathrm{i}}$ and stress $\bar{\mathbf{S}}^{\mathrm{i}}$ in Eq. (4) reduce to

$$\begin{cases} \bar{\mathbf{E}}^{\mathrm{i}} + \bar{\mathbf{E}}^{\mathrm{int}} = \mathcal{A}\left(\mathbf{U}_a^{\mathrm{rm}}\right) \quad \text{and} \quad \bar{\mathbf{E}}^{\mathrm{i}} = \mathcal{A}\left(\mathbf{U}_a^{\mathrm{i}}\right), & \text{(14a)} \\ \bar{\mathbf{S}}^{\mathrm{i}} + \bar{\mathbf{S}}^{\mathrm{int}} = \mu_{\mathrm{ref}}\mathcal{A}\left(\mathbf{T}_a^{\mathrm{rm}}\right) \quad \text{and} \quad \bar{\mathbf{S}}^{\mathrm{i}} = \mu_{\mathrm{ref}}\mathcal{A}\left(\mathbf{T}_a^{\mathrm{i}}\right), & \text{(14b)} \end{cases}$$

where $\mathcal{A}(\boldsymbol{\varphi})$ is a linear functional defined for any function $\boldsymbol{\varphi}$ by

$$\mathcal{A}(\boldsymbol{\varphi}) = \frac{1}{V_0^{\mathrm{i}}}\int_{\partial V_0^{\mathrm{i}}} \boldsymbol{\varphi}\mathbf{X}\mathrm{d}A_0, \tag{15}$$

and $\mathcal{A}$ is independent of the size of the spherical inclusion.

2.4. Concentration tensors for nonlinear heterogeneous materials

2.4.1. Concentration tensors $\mathbf{R}^{\mathrm{c}}$ and $\mathbf{W}^{\mathrm{c}}$

When the material properties c^{i} and c^{i} are sufficiently smooth and the configuration of the SIP does not induce bifurcations or singularities, the invariant relationships $\mathcal{Q}^{\mathrm{rm}}$ and $\mathcal{Q}^{\mathrm{i}}$ in Eqs. (12) and (13) are differentiated at $(c^{\mathrm{rm}}, \mathbf{U}_a^{\mathrm{rm}}, \mathbf{E}^{\infty})$ and $(c^{\mathrm{i}}, \mathbf{U}_a^{\mathrm{i}})$, respectively, with respect to a macroscopic loading parameter (e.g., strain) as

$$\begin{cases} \dot{\mathbf{T}}_a^{\mathrm{rm}} = \dfrac{\partial \mathcal{Q}^{\mathrm{rm}}}{\partial c^{\mathrm{rm}}} \dot{c}^{\mathrm{rm}} + \dfrac{\partial \mathcal{Q}^{\mathrm{rm}}}{\partial \mathbf{U}^{\mathrm{rm}}} \left(\dot{\mathbf{U}}_a^{\mathrm{rm}}\right) + \dfrac{\partial \mathcal{Q}^{\mathrm{rm}}}{\partial \mathbf{E}^{\infty}} \dot{\mathbf{E}}^{\infty}, & \text{(16a)} \\ \dot{\mathbf{T}}_a^{\mathrm{i}} = \dfrac{\partial \mathcal{Q}^{\mathrm{i}}}{\partial c^{\mathrm{i}}} \dot{c}^{\mathrm{i}} + \dfrac{\partial \mathcal{Q}^{\mathrm{i}}}{\partial \mathbf{U}^{\mathrm{i}}} \left(\dot{\mathbf{U}}_a^{\mathrm{i}}\right). & \text{(16b)} \end{cases}$$

The derivations $\partial \mathcal{Q}^{\mathrm{rm}}/\partial \mathbf{U}^{\mathrm{rm}}$, and $\partial \mathcal{Q}^{\mathrm{i}}/\partial \mathbf{U}^{\mathrm{i}}$ can be interpreted as operators that map variations $\dot{\mathbf{U}}_a^{\mathrm{rm}}$, and $\dot{\mathbf{U}}_a^{\mathrm{i}}$ to the resulting increments $\dot{\mathbf{T}}_a^{\mathrm{rm}}$ and $\dot{\mathbf{T}}_a^{\mathrm{i}}$

In the current model and most reported micromechanical models, the inclusion properties are assumed to remain fixed during deformation, i.e.,

$$\dot{c}^{\mathrm{i}} = 0. \tag{17}$$

In contrast, the reference medium in the SIP is a conceptual construct whose properties may evolve during the deformation. Therefore, $\dot{c}^{\mathrm{rm}}$ must be explicitly considered. This reflects a fundamental distinction: the inclusion represents a real physical phase, while the reference medium serves as a fictitious, adaptive construct designed to approximate the surrounding mechanical environment.

To describe the displacement jumps in finite deformation (Tan et al., 2005; Gentieu et al., 2019), we adopt a cohesive zone model (CZM) to represent the interface behavior in this work as a representative example. The traction acting on the interface and the displacement jump $\Delta\mathbf{u} = \mathbf{u}^{\mathrm{rm}} - \mathbf{u}^{\mathrm{i}}$ are related through an interface law $\mathbf{t}^{\mathrm{int}}(\Delta\mathbf{u})$ (Siegmund and Needleman, 1997). To ensure force equilibrium at the interface, we require that

$$\mathbf{t}^{\mathrm{i}}(a) = \mathbf{t}^{\mathrm{rm}}(a) = \mathbf{t}^{\mathrm{int}}(\Delta\mathbf{u}). \tag{18}$$

Right now, Eqs. (2)–(9), (16), and (18) establish the whole computational system as a closed set of governing equations:

$$\begin{pmatrix} \dot{\bar{\mathbf{E}}} \\ \mathbf{0} \\ \dfrac{\partial \mathcal{Q}^{\mathrm{rm}}}{\partial c^{\mathrm{rm}}} \dot{c}^{\mathrm{rm}} \end{pmatrix} = \mathbf{K}_0 \begin{pmatrix} \dot{\mathbf{E}}^{\infty} \\ \dot{\mathbf{U}}_a^{\mathrm{rm}} \\ \dot{\mathbf{U}}_a^{\mathrm{i}} \end{pmatrix} \quad \text{and} \quad \frac{\dot{\mathbf{S}}}{\mu_{\mathrm{ref}}} = \mathbf{l}_0 \begin{pmatrix} \dot{\mathbf{E}}^{\infty} \\ \dot{\mathbf{U}}_a^{\mathrm{rm}} \\ \dot{\mathbf{U}}_a^{\mathrm{i}} \end{pmatrix}, \tag{19}$$

where arrays $\mathbf{K}_0$ and $\mathbf{l}_0$ read

$$\mathbf{K}_0 = \begin{pmatrix} v^{\mathrm{m}} w^{\mathrm{rm}} \mathbf{I} & (v^{\mathrm{m}} w^{\mathrm{i}} + v^{\mathrm{i}}) \mathcal{A} & \mathbf{0} \\ \mathbf{0} & \dfrac{a}{\mu_{\mathrm{ref}}} \dfrac{\partial \mathbf{t}^{\mathrm{int}}}{\partial \Delta\mathbf{u}} & -\dfrac{a}{\mu_{\mathrm{ref}}} \dfrac{\partial \mathbf{t}^{\mathrm{int}}}{\partial \Delta\mathbf{u}} - \dfrac{\partial \mathcal{Q}^{\mathrm{i}}}{\partial \mathbf{U}^{\mathrm{i}}} \\ -\dfrac{\partial \mathcal{Q}^{\mathrm{rm}}}{\partial \mathbf{E}^{\infty}} & -\dfrac{\partial \mathcal{Q}^{\mathrm{rm}}}{\partial \mathbf{U}^{\mathrm{rm}}} & \dfrac{\partial \mathcal{Q}^{\mathrm{i}}}{\partial \mathbf{U}^{\mathrm{i}}} \end{pmatrix}, \tag{20}$$

and

$$\mathbf{l}_0 = \begin{pmatrix} v^{\mathrm{m}} w^{\mathrm{rm}} \dfrac{\bar{\mathbf{L}}^{\mathrm{m}}}{\mu_{\mathrm{ref}}} & v^{\mathrm{m}} w^{\mathrm{i}} \dfrac{\bar{\mathbf{L}}^{\mathrm{m}}}{\mu_{\mathrm{ref}}} : \mathcal{A} & v^{\mathrm{i}} \dfrac{\partial \mathcal{Q}^{\mathrm{i}}}{\partial \mathbf{U}^{\mathrm{i}}} : \mathcal{A} \end{pmatrix}. \tag{21}$$

Here, w^{rm} and w^{i} represent the coefficients of $\dot{\bar{\mathbf{E}}}^{\mathrm{m}} = w^{\mathrm{rm}} \dot{\mathbf{E}}^{\infty} + \sum_k w_k^{\mathrm{i}} (\dot{\bar{\mathbf{E}}}_k^{\mathrm{i}} + \dot{\bar{\mathbf{E}}}_k^{\mathrm{int}})$, which can be calculated from Eqs. (4) and (9). The interaction between $\mathcal{A}$ and the following variables is not in the form of product, but in the form of functional operation $\mathcal{A}(\bullet)$, which is determined based on Eq. (15). For systems involving multiple inclusion types, the formulation can be extended by increasing the array dimensionality.

Recalling Eq. (8) that $\bar{\mathbf{E}}^{\mathrm{i}} = \mathcal{G}^{\mathrm{i}}(c^{\mathrm{rm}}, \mathbf{E}^{\infty})$ and $\bar{\mathbf{E}}^{\mathrm{int}} = \mathcal{G}^{\mathrm{int}}(c^{\mathrm{rm}}, \mathbf{E}^{\infty})$, the derivatives of $\mathcal{G}^{\mathrm{i}}$ and $\mathcal{G}^{\mathrm{int}}$ can be extracted from Eqs. (19) and (20). Following the methodology introduced in Section 2.2.2 and utilizing a standard least-square procedure, we obtain the evolution of the reference medium property as

$$\dot{c}^{\mathrm{rm}} = \frac{\partial w^{c}}{\partial c^{\mathrm{h}}} \left[\left(\frac{\partial \Psi^{\mathrm{h}}}{\partial c^{\mathrm{h}}} \right)^{\mathrm{T}} : \frac{\partial \Psi^{\mathrm{h}}}{\partial c^{\mathrm{h}}} \right]^{-1} \left(\frac{\partial \Psi^{\mathrm{h}}}{\partial c^{\mathrm{h}}} \right)^{\mathrm{T}} : \left[\mathbf{l}_{\mathrm{r}} \begin{pmatrix} \dot{\mathbf{E}}^{\infty} \\ \dot{\mathbf{U}}_a^{\mathrm{rm}} \\ \dot{\mathbf{U}}_a^{\mathrm{i}} \end{pmatrix} \right], \tag{22}$$

where $\mathbf{l}_{\mathrm{r}}$, defined in Eq. (C.3), is the revised array about modulus considering macroscopic property variation

Utilizing Eq. (14), we organize Eqs. (19)–(22) into the form as Eq. (5) that $\dot{\bar{\mathbf{E}}}^{\mathrm{i}} = \mathbf{R}^{\mathrm{c}} : \dot{\bar{\mathbf{E}}}$ and $\dot{\bar{\mathbf{S}}}^{\mathrm{i}} = \mathbf{U}^{\mathrm{c}} : \dot{\bar{\mathbf{S}}}$. The concentration tensors for the inclusion $\mathbf{R}^{\mathrm{c}}$ and interface $\mathbf{W}^{\mathrm{c}}$ can be expressed as

$$\begin{cases} \mathbf{R}^{\mathrm{c}} = \dfrac{1}{\Delta_{\mathbf{K}_{\mathrm{r}}}} \dfrac{a}{\mu_{\mathrm{ref}}} \mathcal{A} \left(\dfrac{\partial \mathbf{t}^{\mathrm{int}}}{\partial \Delta\mathbf{u}} \right)^{\mathrm{T}} \mathbf{P}, & \text{(23a)} \\ \mathbf{W}^{\mathrm{c}} = \dfrac{1}{\Delta_{\mathbf{K}_{\mathrm{r}}}} \mathcal{A} \left(\dfrac{\partial \mathcal{Q}^{\mathrm{i}}}{\partial \mathbf{U}^{\mathrm{i}}} \right)^{\mathrm{T}} \mathbf{P}, & \text{(23b)} \end{cases}$$

where

$$\mathbf{P} = \frac{\partial \mathcal{Q}^{\mathrm{rm}}}{\partial \mathbf{E}^{\infty}} + v^{\mathrm{m}} w^{\mathrm{rm}} \frac{\partial \mathcal{Q}^{\mathrm{rm}}}{\partial c^{\mathrm{rm}}} \frac{\partial w^{c}}{\partial c^{\mathrm{h}}} \left[\left(\frac{\partial \Psi^{\mathrm{h}}}{\partial c^{\mathrm{h}}} \right)^{\mathrm{T}} : \frac{\partial \Psi^{\mathrm{h}}}{\partial c^{\mathrm{h}}} \right]^{-1} \left(\frac{\partial \Psi^{\mathrm{h}}}{\partial c^{\mathrm{h}}} \right)^{\mathrm{T}} : \left(\frac{\bar{\mathbf{L}}^{\mathrm{m}}}{\mu_{\mathrm{ref}}} - \frac{\partial \Psi^{\mathrm{h}}}{\partial \bar{\mathbf{E}}} \right), \tag{24}$$

and $\Delta_{\mathbf{K}_{\mathrm{r}}}$ is the determinant of the following array $\mathbf{K}_{\mathrm{r}}$

$$\mathbf{K}_{\mathrm{r}} = \mathbf{K}_0 - \begin{pmatrix} \mathbf{0} \\ \mathbf{0} \\ \mathbf{1} \end{pmatrix} \frac{\partial \mathcal{Q}^{\mathrm{rm}}}{\partial c^{\mathrm{rm}}} \frac{\partial w^{c}}{\partial c^{\mathrm{h}}} \left[\left(\frac{\partial \Psi^{\mathrm{h}}}{\partial c^{\mathrm{h}}} \right)^{\mathrm{T}} : \frac{\partial \Psi^{\mathrm{h}}}{\partial c^{\mathrm{h}}} \right]^{-1} \left(\frac{\partial \Psi^{\mathrm{h}}}{\partial c^{\mathrm{h}}} \right)^{\mathrm{T}} : \mathbf{l}_{\mathrm{r}}. \tag{25}$$

With the knowledge of $\mathbf{R}^{\mathrm{c}}$ and $\mathbf{W}^{\mathrm{c}}$ in Eq. (23), the effective tangent modulus tensor $\mathbf{L}^{\mathrm{h}}$ is finally obtained using Eq. (7).

The SIP framework developed above provides the analytical formulas for $\mathbf{L}^{\mathrm{h}}$. However, the crucial invariant relations $\mathcal{Q}^{\mathrm{rm}}$ and $\mathcal{Q}^{\mathrm{i}}$ cannot be determined directly within the SIP theory. To supply this necessary closure, we employ PGNNs to learn the $\mathcal{Q}$ relations. The PGNNs are trained as surrogates using a problem-independent database generated from independent finite element simulations, as detailed in Section 3.

In practice of our computational analysis integrating PGNNs, the determinization of $\mathbf{R}^{\mathrm{c}}$ and $\mathbf{W}^{\mathrm{c}}$ involves discretizations of the quantities $\mathbf{t}^{\mathrm{int}}$, $\Delta\mathbf{u}$, $\mathcal{Q}^{\mathrm{rm}}$, and $\mathcal{Q}^{\mathrm{i}}$. Since $\mathbf{t}^{\mathrm{int}} = \mu_{\mathrm{ref}} \mathbf{T}_a^{\mathrm{rm}} = \mu_{\mathrm{ref}} \mathbf{T}_a^{\mathrm{i}}$, $\Delta\mathbf{u} = \mathbf{u}^{\mathrm{rm}} - \mathbf{u}^{\mathrm{i}} = a(\mathbf{U}_a^{\mathrm{rm}} - \mathbf{U}_a^{\mathrm{i}})$, $\mathbf{T}^{\mathrm{rm}}(R) = \mathcal{Q}^{\mathrm{rm}}(c^{\mathrm{rm}}, \mathbf{U}^{\mathrm{rm}}(R))$, and $\mathbf{T}^{\mathrm{i}}(R) = \mathcal{Q}^{\mathrm{i}}\left(c^{\mathrm{i}}, \mathbf{U}^{\mathrm{i}}(R)\right)$, all discretizations eventually reduce to the discretizations of $\mathbf{U}^{\mathrm{i}}(R)$, $\mathbf{U}^{\mathrm{rm}}(R)$, $\mathbf{T}^{\mathrm{i}}(R)$, and $\mathbf{T}^{\mathrm{rm}}(R)$. The discretization processes are described in the following section.

Once the discretization is completed, the evolution of the reference medium property $\partial c^{\mathrm{rm}}/\partial \bar{\mathbf{E}}$ and the concentration tensors $\mathbf{R}^{\mathrm{c}}$ and $\mathbf{W}^{\mathrm{c}}$ are determined simultaneously through numerical computation, and the effective tangent modulus $\mathbf{L}^{\mathrm{h}}$ in Eq. (7) is then obtained from the concentration tensors. Furthermore, the distribution $\mathbf{U}_a^{\mathrm{i}}$ and $(\mathbf{U}_a^{\mathrm{rm}} - \mathbf{U}_a^{\mathrm{i}})$ obtained in the computation reveal the deformation patterns of the inclusions and interfaces.

Based on the micromechanical formulation of the effective tangent modulus $\mathbf{L}^{\mathrm{h}}$, in which the key components of the expressions are represented by neural networks, the stress–strain response is computed using a fourth-order Runge–Kutta method (Shampine and Reichelt, 1997). This framework thus eliminates the need for repeated model construction and expensive finite element method (FEM) simulations.

2.4.2. Discretization

In the SIP (Fig. 3), the displacement and traction distributions are periodic functions of Θ and Φ. The x, y, and z components of the displacements and tractions $\mathbf{U}^{\mathrm{i}}(R)$, $\mathbf{U}^{\mathrm{rm}}(R)$, $\mathbf{T}^{\mathrm{i}}(R)$, and $\mathbf{T}^{\mathrm{rm}}(R)$ (uniformly denoted by $\boldsymbol{\varphi}$) are discretized via the Fourier series

$$\varphi_\beta^{\mathrm{F}} = \sum_{m=0}^{m_{\max}} \sum_{n=0}^{n_{\max}} \varphi_\beta^{(m,n)} \left[A_\beta^{(n)} \cos(n\Phi) + B_\beta^{(n)} \sin(n\Phi) \right] \left[C_\beta^{(m)} \cos(m\Theta) + D_\beta^{(m)} \sin(m\Theta) \right], \tag{26}$$

where $\beta = x$, y, or z. We denote the sets of coefficients by $\{U\}$ and $\{T\}$ for displacements $U_\beta^{(m,n)}(R)$ and tractions $T_\beta^{(m,n)}(R)$, respectively. Under this Fourier discretization and decomposition, the functional $\mathcal{A}(\boldsymbol{\varphi}^{\mathrm{F}})$ becomes Eq. (B.3).

Then, the mappings $\mathcal{Q}^{\mathrm{rm}}$ in Eq. (12) and $\mathcal{Q}^{\mathrm{i}}$ in Eq. (13) expressed as multivariate functions of the Fourier coefficients: $\{T^{\mathrm{rm}}\} = \mathcal{Q}^{\mathrm{rm}}(c^{\mathrm{rm}}, \{U^{\mathrm{rm}}\}, \mathbf{E}^{\infty})$ and $\{T^{\mathrm{i}}\} = \mathcal{Q}^{\mathrm{i}}(c^{\mathrm{i}}, \{U^{\mathrm{i}}\})$. Similarly, the mappings $\partial\mathcal{Q}^{\mathrm{rm}}/\partial c^{\mathrm{rm}}$, $\partial\mathcal{Q}^{\mathrm{rm}}/\partial \mathbf{U}^{\mathrm{rm}}$, $\partial\mathcal{Q}^{\mathrm{rm}}/\partial \mathbf{E}^{\infty}$, $\partial\mathcal{Q}^{\mathrm{i}}/\partial c^{\mathrm{i}}$, and $\partial\mathcal{Q}^{\mathrm{i}}/\partial \mathbf{U}^{\mathrm{i}}$ are discretized as the corresponding derivatives of these functions, that is, $\partial Q^{\mathrm{rm}}/\partial c^{\mathrm{rm}}$, $\partial Q^{\mathrm{rm}}/\partial\{U^{\mathrm{rm}}\}$, $\partial Q^{\mathrm{rm}}/\partial \mathbf{E}^{\infty}$, $\partial Q^{\mathrm{i}}/\partial c^{\mathrm{i}}$, and $\partial Q^{\mathrm{i}}/\partial\{U^{\mathrm{i}}\}$. The calculation of $\partial \mathbf{t}^{\mathrm{int}}/\partial\Delta\mathbf{u}$ for the CZM is likewise converted to a discrete form, as shown in Eq. (B.4).

3. Calculation implementation

3.1. Data generation

To generate training data for the neural network, we use composites of incompressible hyperelastic materials as primary illustrative examples. The normalized strain energy density of such materials is expressed in a general form as $\psi = \sum_{i,j} c_{ij}(I_1 - 3)^i (I_2 - 3)^j$, where c_{ij} are dimensionless material parameters. Here, $I_1(\mathbf{E})$ and $I_2(\mathbf{E})$ denote the first and second invariants of the right Cauchy–Green tensor $\mathbf{C} = \mathbf{F}^{\mathrm{T}} \cdot \mathbf{F} = (\mathbf{E} + \mathbf{I}) \cdot (\mathbf{E} + \mathbf{I})$, respectively, with $\mathbf{E}$ as the engineering strain. The invariants I_1 and I_2 are defined consistently for all phases, including inclusions ($I_1^{\mathrm{i}} = I_1(\mathbf{E}^{\mathrm{i}})$ and $I_2^{\mathrm{i}} = I_2(\mathbf{E}^{\mathrm{i}})$), matrix ($I_1^{\mathrm{m}} = I_1(\mathbf{E}^{\mathrm{m}})$ and $I_2^{\mathrm{m}} = I_2(\mathbf{E}^{\mathrm{m}})$), reference medium ($I_1^{\mathrm{rm}} = I_1(\mathbf{E}^{\mathrm{rm}})$ and $I_2^{\mathrm{rm}} = I_2(\mathbf{E}^{\mathrm{rm}})$), and the homogenized composite ($I_1^{\mathrm{h}} = I_1(\bar{\mathbf{E}})$ and $I_2^{\mathrm{h}} = I_2(\bar{\mathbf{E}})$).

While the theoretical framework developed above, including the design of the PGNNs, is general and directly applicable to fully three-dimensional problems, in this work we validate it under axisymmetric loading conditions, such as uniaxial tension and equi-biaxial loading in the circumferential plane. These conditions provide a canonical benchmark that facilitates systematic parametric analysis while retaining the essential physics necessary for meaningful validation. To generate data for the nonlinear deformation field, we construct a finite element model of the representative SIP with an axisymmetric configuration in Abaqus (Fig. 3), where the x-axis denotes the axial coordinate and ρ represents the radial coordinate in the y–z plane.

Both the spherical inclusion and the surrounding reference medium are modeled as hyperelastic solids. As described in Section 2.3.1, the reference medium is assigned different material parameters to investigate the material property influence. Specifically, a Mooney–Rivlin model (Rivlin and Saunders, 1951) is adopted for the isotropic reference medium, with the normalized strain energy density $\psi = c_{10}(I_1 - 3) + c_{01}(I_2 - 3)$. Because ψ is proportional to the stress in the hyperelastic constitutive relation, scaling both parameters c_{10} and c_{01} by the same factor leads to the same proportional scaling of the stress. Thus, one parameter

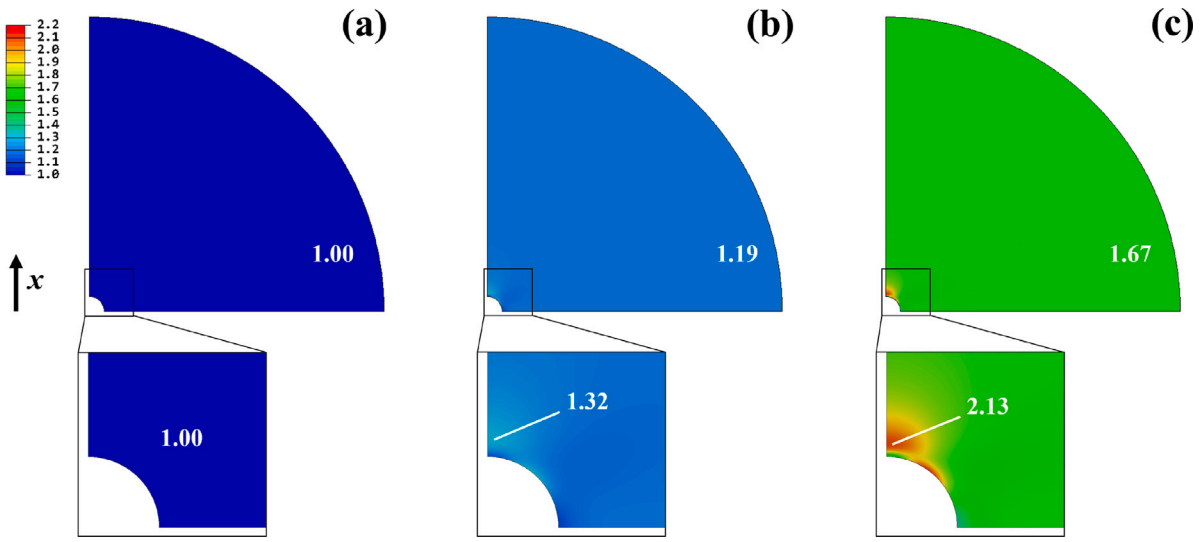

Fig. 4. The equivalent shear modulus G_{eq} distribution of the reference medium at far-field strains of 0 (a), 0.5 (b), and 1 (c). The modulus exhibits dual heterogeneity: spatial variation due to geometry and deformation-induced evolution. Note that for hyperelastic materials, the tangent modulus is not an intrinsic material constant but a state-dependent quantity that varies with the local strain. Accordingly, the tangent modulus field reflects the varying mechanical response under deformation.

(e.g., c_{10}) can be fixed without losing generality, and the actual stress can then be recovered by rescaling the normalized result with the corresponding factor of the original coefficients. In this work, c_{10} is fixed at 0.5, while c_{01} varies from 0 to 0.5. The isotropic inclusion is modeled using the neo-Hookean model (Treloar, 1943), with the normalized strain energy density $\psi = c(I_1 - 3)$, where c ranges from 0.1 to 100.

To realize far-field strains along the axisymmetric loading direction ranging from −50% compression to 100% tension, prescribed displacements are applied to the outer boundary of the reference medium. Following Chen et al. (2024), the outer radius of the reference medium is set to $R_b^{rm} = 20a$, which ensures a sufficiently large domain to approximate an infinite reference medium. The boundary conditions under uniaxial loading are described in detail in Supplementary Materials.

The computational domain is meshed with hybrid-enhanced CAX4RH and CAX3H elements. The investigated mechanical field is confined to an annular region $a/2 \le R \le 2a$. For each set of boundary conditions, the deformation field is computed, and a total of 320236 data points (including displacement, stress, and deformation gradient) are extracted. The first Piola–Kirchhoff stress $\mathbf{S}$ at different points are then computed.

As one of the examples for data generation, Fig. 4 shows the spatial distribution of the equivalent shear modulus G_{eq} in the reference medium at selected far-field strain levels $E_{xx}^{\infty} = 0$, 0.5, and 1, where E_{xx}^{∞} is the normal engineering strain in the x-direction, corresponding the applied displacement boundary condition. As a robust measure of local shear stiffness, G_{eq} is defined as the Frobenius norm of the deviatoric part of $2(\partial \mathbf{S}^{(2)}/\partial \mathbf{C})$ (Holzapfel, 2000), where $\mathbf{S}^{(2)}$ denotes the second Piola–Kirchhoff stress. The reference medium parameters are $c_{10} = 0.5$ and $c_{01} = 0$, while $c = 2.5$ is used for the inclusion (not shown in Fig. 4). The modulus field is evaluated following the Abaqus User Subroutines Reference Manual and normalized by the initial shear modulus of the undeformed reference medium. As shown in Fig. 4a, the modulus of the undeformed reference medium is initially uniform, ensuring that this model recovers the classical limit at infinitesimal deformation. With varying load at the boundary, G_{eq} in the reference medium changes accordingly. In regions far from the inclusion, the modulus remains nearly uniform due to the large reference domain, whereas near the inclusion, where training data are collected, it becomes increasingly non-uniform, exhibiting spatial fluctuations exceeding 40% (Fig. 4c). This result highlights the highly non-uniform and deformation-dependent nature of the tangent modulus field, a hallmark of nonlinear heterogeneous materials where material nonlinearity and strain localization couple to produce complex mechanical responses.

3.2. Neural network training

This section introduces the architecture and training procedure of the neural network. Prior to training, the data are preprocessed. In the deformation field generated by the finite element model, the distribution $\boldsymbol{\varphi}$ (e.g., displacements and tractions) on a spherical surface of radius R, is approximated by a Fourier series representation $\boldsymbol{\varphi}^{F}$. The Fourier coefficients are determined by minimizing the following residual

$$Res = \int_0^{\pi} \int_0^{2\pi} |\boldsymbol{\varphi} - \boldsymbol{\varphi}^{F}|^2 R^2 \sin\Theta \mathrm{d}\Phi \mathrm{d}\Theta. \tag{27}$$

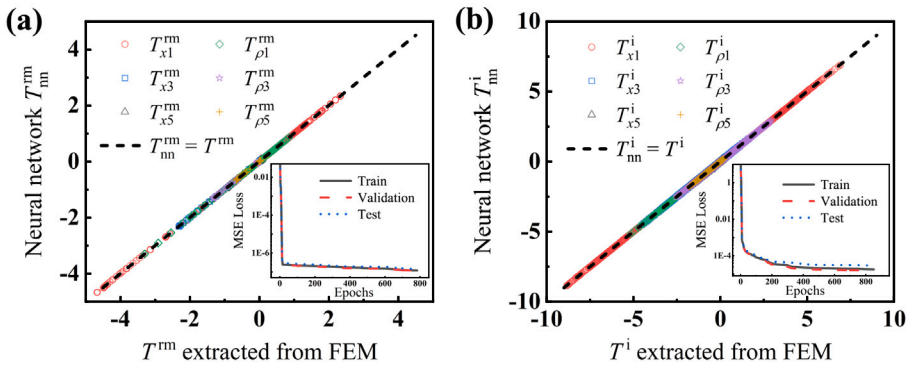

Fig. 5. Training results of the neural network for the nonlinear invariant relations: (a) Q^{rm} and (b) Q^{i}. The neural network–predicted traction responses T_{nn} are compared with FEM-derived values, with distinct symbols marking the six coefficients of traction. Insets show the MSE loss curves for training, validation, and test datasets over the epochs.

The least-squares method is employed to obtain the optimal coefficients $\{T^{\mathrm{rm}}\}$, $\{U^{\mathrm{rm}}\}$, $\{T^{\mathrm{i}}\}$, and $\{U^{\mathrm{i}}\}$, with details provided in Appendix B. $m_{\max} = n_{\max} = 3$ are taken.

We adopt multi-layer perceptron type neural networks $Q^{\mathrm{rm}}_{\mathrm{nn}}$ and $Q^{\mathrm{i}}_{\mathrm{nn}}$ to approximate the invariant relations $\{T^{\mathrm{rm}}\} = Q^{\mathrm{rm}}(c^{\mathrm{rm}}, \{U^{\mathrm{rm}}\}, \mathbf{E}^{\infty})$ and $\{T^{\mathrm{i}}\} = Q^{\mathrm{i}}(c^{\mathrm{i}}, \{U^{\mathrm{i}}\})$. It functions as a composite mapping $\vec{x}^{k+1} = f_{\mathrm{a}}((W^k)^{\mathrm{T}} \cdot \vec{x}^k + \vec{b}^k)$, where the data vector $\vec{x}^k$ at the kth layer undergoes a linear transformation followed by a nonlinear activation f_{a}, producing the input to the next layer. Here, $\vec{b}^k$ and W^k represent bias parameters and weight coefficients, respectively. We select the sigmoid activation function, $f_{\mathrm{a}}(y) = 1/(1+e^{-y})$, whose derivative, required in the chain rule for backpropagation, is given by

$$\frac{\mathrm{d}f_{\mathrm{a}}(y)}{\mathrm{d}y} = \frac{e^{-y}}{(1+e^{-y})^2} = f_{\mathrm{a}}(y)\left[1 - f_{\mathrm{a}}(y)\right], \tag{28}$$

which further facilitate a simplified automatic differentiation scheme to efficiently compute $\partial Q^{\mathrm{rm}}/\partial c^{\mathrm{rm}}$, $\partial Q^{\mathrm{rm}}/\partial \{U^{\mathrm{rm}}\}$, $\partial Q^{\mathrm{rm}}/\partial \mathbf{E}^{\infty}$, $\partial Q^{\mathrm{i}}/\partial c^{\mathrm{i}}$, and $\partial Q^{\mathrm{i}}/\partial \{U^{\mathrm{i}}\}$.

The training procedure aims to optimize all network parameters W^k and $\vec{b}^k (k = 0, 1, 2, \ldots)$ by minimizing the mean squared error (MSE) loss:

$$Loss^{\mathrm{i}} = \left\| \left\{T^{\mathrm{i}}\right\} - Q^{\mathrm{i}}_{\mathrm{nn}}\left(c^{\mathrm{i}}, \left\{U^{\mathrm{i}}\right\}\right)\right\|^2, \quad \text{and} \quad Loss^{\mathrm{rm}} = \left\| \left\{T^{\mathrm{rm}}\right\} - Q^{\mathrm{rm}}_{\mathrm{nn}}\left(c^{\mathrm{rm}}, \left\{U^{\mathrm{rm}}\right\}, \mathbf{E}^{\infty}\right)\right\|^2. \tag{29}$$

After pre-processing, a total of 2568 data sets were used and divided into training (70%), validation (15%), and testing (15%) subsets. The network was trained in MATLAB's Neural Network Toolbox using the Levenberg–Marquardt optimization algorithm (Hagan and Menhaj, 1994). The entire workflow, including data pre-processing and training, was completed in about 2 min.

To evaluate the fitting performance of the neural networks, the regression results are presented in Fig. 5. The predicted traction coefficients T_{nn} are compared with those obtained directly from FEM. The insets in the bottom right of each panel depict the evolution of the MSE loss for the training, validation, and test datasets over the training epochs. After approximately 800 epochs, the MSE falls below 10^{-4}. These results indicate that the networks for both the inclusion and the reference medium achieve accurate fits. Consequently, the nonlinear functions Q^{rm} and Q^{i} can be reliably represented by $Q^{\mathrm{rm}}_{\mathrm{nn}}$ and $Q^{\mathrm{i}}_{\mathrm{nn}}$, respectively. All computations were performed on a personal computer with an Intel Core i7-10700 CPU (8 cores) using two processors.

Fig. 6 illustrates the surfaces of the nonlinear relations for Q^{rm} and Q^{i}. The material parameters of the hyperelastic reference medium and inclusion are set to $c^{\mathrm{rm}}_{10} = 0.5$, $c^{\mathrm{rm}}_{01} = 0$, and $c^{\mathrm{i}} = 0.5$, with the far-field strain of the reference medium fixed at $\mathbf{E}^{\infty} = \mathbf{0}$. The dominant parameters, namely the first-order coefficients U_{x1}, $U_{\rho 1}$, T_{x1}, and $T_{\rho 1}$ are examined. The nonlinear nature of Q^{rm} and Q^{i} results in complex surface representations. Under linear small-deformation conditions, the surfaces are expected to reduce to planar forms. Since the reference medium and the inclusion are located on opposite sides of the spherical surface where Q^{rm} and Q^{i} are defined, the nonlinear response of the reference medium is opposite to that of the inclusion. Furthermore, because the reference medium is much larger than the inclusion, its nonlinear behavior is less pronounced.

4. Numerical results

This section presents numerical results using the proposed nonlinear micromechanical framework. Section 4.1 provides a benchmark evaluation under classical experimental conditions and compares different micromechanics models. Section 4.2 examines the reference medium, focusing on (i) variations in its material properties and (ii) spatially non-uniform modulus distributions. Section 4.3 evaluates the method's adaptability to diverse nonlinear isotropic inclusions, matrices, and interfaces—including mixed inclusion types—using the same trained neural networks.

For all cases of uniaxial tension or compression, either a macroscopic engineering (nominal) strain ε or an engineering stress S is applied along the loading direction.

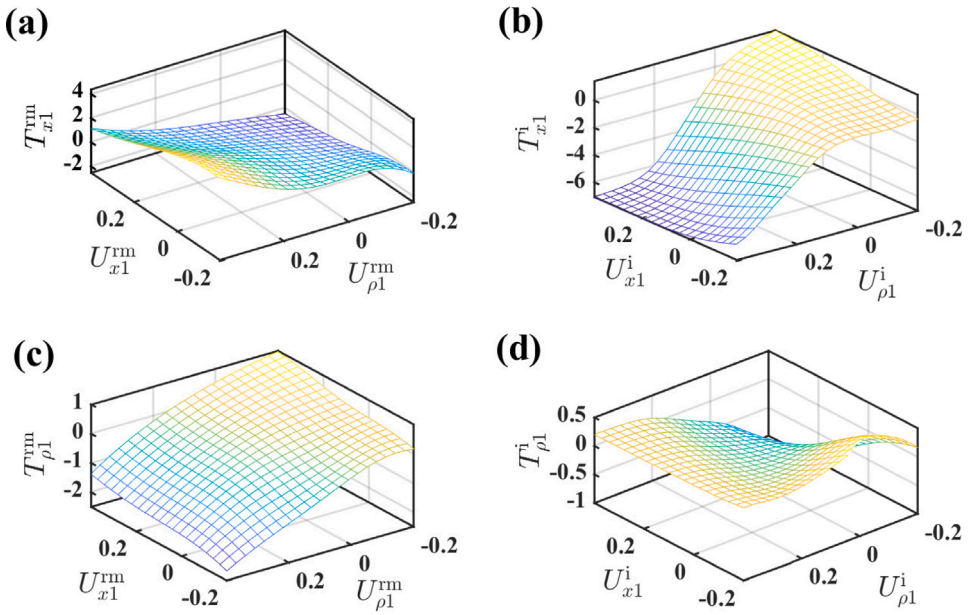

Fig. 6. Surface representation of nonlinear relationships Q. Panels (a) and (c) show the variation surfaces of the two components of T with respect to the two components of U for the inclusion, while panels (b) and (d) correspond to the reference medium. Only the first-order components are considered.

4.1. Estimation by nonlinear micromechanical schemes

In regular micromechanical methods, Eq. (9) is formulated as $\mathbf{E}^{\infty} = w^{\bar{\mathbf{E}}^{\mathrm{m}}}\bar{\mathbf{E}}^{\mathrm{m}} + w^{\bar{\mathbf{E}}}\bar{\mathbf{E}}$, where $w^{\bar{\mathbf{E}}^{\mathrm{m}}}$ and $w^{\bar{\mathbf{E}}}$ are coefficients. Using Eq. (4), the average matrix strain $\bar{\mathbf{E}}^{\mathrm{m}}$ can be written as

$$\bar{\mathbf{E}}^{\mathrm{m}} = w^{\mathrm{rm}}\mathbf{E}^{\infty} + \sum_k w^{\mathrm{i}}_k(\bar{\mathbf{E}}^{\mathrm{i}}_k + \bar{\mathbf{E}}^{\mathrm{int}}_k), \tag{30}$$

where coefficients $w^{\mathrm{rm}} = 1/(w^{\bar{\mathbf{E}}^{\mathrm{m}}} + v^{\mathrm{m}}w^{\bar{\mathbf{E}}})$ and $w^{\mathrm{i}}_k = -v^{\mathrm{i}}_k w^{\bar{\mathbf{E}}}/(w^{\bar{\mathbf{E}}^{\mathrm{m}}} + v^{\mathrm{m}}w^{\bar{\mathbf{E}}})$ are subsequently used in deriving the tangent modulus (Appendix C). In the following numerical results in Section 4, unless stated otherwise, we take $\mathbf{E}^{\infty} = \bar{\mathbf{E}}$ ($w^{\bar{\mathbf{E}}^{\mathrm{m}}} = 0$ and $w^{\bar{\mathbf{E}}} = 1$) and $c^{\mathrm{rm}} = c^{\mathrm{h}}$ with $\Psi^{\mathrm{rm}} = \Psi^{\mathrm{h}}$.

We apply the proposed neural-network-enhanced method with evolving reference medium (ENM) to a benchmark composite material studied by Mullins and Tobin (1965), consisting of rigid inclusions with perfect interfacial bonding embedded in a Mooney–Rivlin elastomer matrix with material parameters $\mu_{\mathrm{ref}}c_{10} = 1.70$ MPa and $\mu_{\mathrm{ref}}c_{01} = 0.69$ MPa. Four inclusion volume fractions are considered: $v^{\mathrm{i}} = 0.0535$, 0.084, 0.1382, and 0.2085. The composite is subjected to uniaxial tension ε up to 100% engineering strain.

The homogenized material and the isotropic reference medium are both described by the Mooney–Rivlin strain energy density $\psi^{\mathrm{h}} = c^{\mathrm{h}}_{10}(I^{\mathrm{h}}_1 - 3) + c^{\mathrm{h}}_{01}(I^{\mathrm{h}}_2 - 3)$ and $\psi^{\mathrm{rm}} = c^{\mathrm{rm}}_{10}(I^{\mathrm{rm}}_1 - 3) + c^{\mathrm{rm}}_{01}(I^{\mathrm{rm}}_2 - 3)$, where coefficients $c^{\mathrm{h}}_{10}(\bar{\mathbf{E}})$, $c^{\mathrm{h}}_{01}(\bar{\mathbf{E}})$, $c^{\mathrm{rm}}_{10}(\bar{\mathbf{E}})$, and $c^{\mathrm{rm}}_{01}(\bar{\mathbf{E}})$ vary with the macroscopic strain $\bar{\mathbf{E}}$.

Fig. 7a shows the predicted tangent modulus $L^{\mathrm{h}} = \mathrm{d}S/\mathrm{d}\varepsilon$ using the ENM method. Higher inclusion volume fractions lead to larger tangent moduli. While the modulus decreases with strain, the reduction becomes less pronounced at large deformation. Fig. 7b compares the ENM-predicted nominal stress S with experimental data (symbols), with the pure matrix response shown as a dotted line for reference. The predictions align closely with experimental results across all volume fractions, demonstrating the accuracy of the proposed ENM scheme.

We also examine two degenerate cases of the ENM scheme. Setting $\mathbf{E}^{\infty} = \bar{\mathbf{E}}$ and $c^{\mathrm{rm}} = c^{\mathrm{m}}$ with $\Psi^{\mathrm{rm}} = \Psi^{\mathrm{m}}$, we have the nonlinear dilute (ND) method. Alternatively, taking $\mathbf{E}^{\infty} = \bar{\mathbf{E}}^{\mathrm{m}}$ ($w^{\bar{\mathbf{E}}^{\mathrm{m}}} = 1$ and $w^{\bar{\mathbf{E}}} = 0$) and $c^{\mathrm{rm}} = c^{\mathrm{m}}$ with $\Psi^{\mathrm{rm}} = \Psi^{\mathrm{m}}$, we have the nonlinear Mori–Tanaka (NMT) method. Based on Eq. (30), their tangent moduli, obtained from Eq. (10), are

$$\mathbf{L}^{\mathrm{h}} = \bar{\mathbf{L}}^{\mathrm{m}} - \sum_k v^{\mathrm{i}}_k(\bar{\mathbf{L}}^{\mathrm{m}} - \bar{\mathbf{L}}^{\mathrm{i}}_k) : \frac{\partial \mathcal{G}^{\mathrm{i}}_k}{\partial \mathbf{E}^{\infty}} \quad \text{for the ND method,} \tag{31}$$

and

$$\mathbf{L}^{\mathrm{h}} = \left[v^{\mathrm{m}}\bar{\mathbf{L}}^{\mathrm{m}} + \sum_k v^{\mathrm{i}}_k \bar{\mathbf{L}}^{\mathrm{i}}_k : \frac{\partial \mathcal{G}^{\mathrm{i}}_k}{\partial \mathbf{E}^{\infty}}\right] : \left[v^{\mathrm{m}}\mathbf{I} + \sum_k v^{\mathrm{i}}_k \frac{\partial \mathcal{G}^{\mathrm{i}}_k}{\partial \mathbf{E}^{\infty}}\right]^{-1} \quad \text{for the NMT method.} \tag{32}$$

In the limit of linear elasticity, $\partial \mathcal{G}^{\mathrm{i}}_k/\partial \mathbf{E}^{\infty}$ reduce to the classical strain concentration tensors, and the ND and NMT schemes recover the effective modulus expressions of Eshelby (1957) and Mori and Tanaka (1973), respectively.

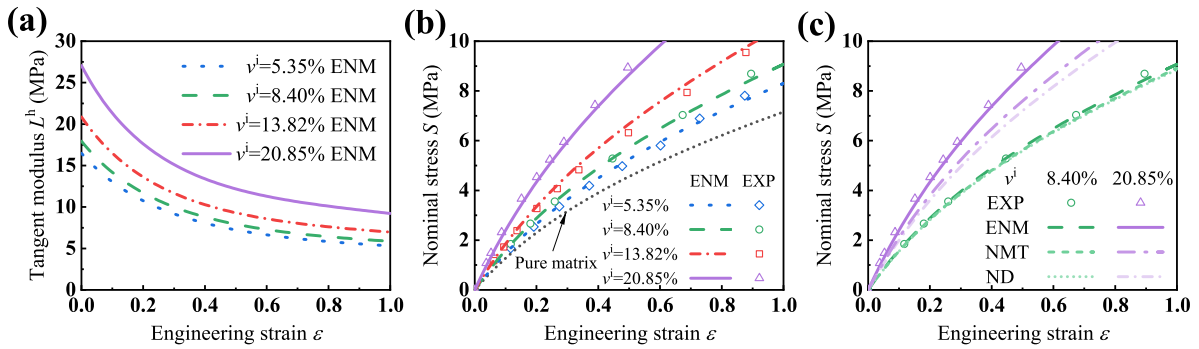

Fig. 7. (a) Tangent modulus evolution of the particle-reinforced composites with a Mooney–Rivlin matrix and rigid spherical inclusions at various volume fractions, based on ENM predictions. (b) Stress–strain curves predicted by ENM compared with experimental data from Mullins and Tobin (1965). The dashed line indicates the response of the pure matrix. (c) Comparison of predictions from ENM, NMT, and ND.

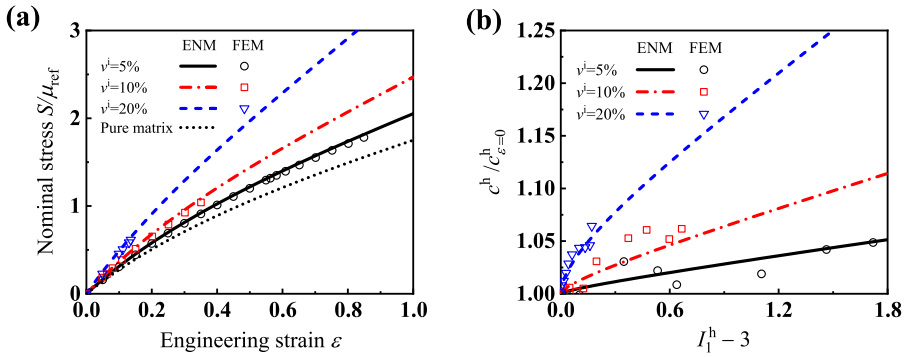

Fig. 8. Stress–strain responses predicted by the ENM, compared with FEM results reported in Guo et al. (2014). Three cases with rigid inclusions at volume fractions $v^i = 0.05$, 0.1, and 0.2, all assuming perfect interfacial bonding. (b) Variation of the material parameter c^h normalized by its initial value at $\varepsilon = 0$.

Fig. 7c compares the predictions of the ENM, NMT, and ND schemes. At a low volume fraction (e.g., 0.084), all three methods agree well with experiments. However, at a high volume fraction (e.g., 0.2085), ENM shows superior accuracy. The NMT method tends to underestimate the composite modulus in this regime, likely due to its intrinsic limitations when applied to densely packed inclusions. By contrast, ENM treats the reference medium as the actual homogenized material, enforcing a modulus equivalence that better reflects the mechanical environment surrounding the inclusions.

4.2. Deformation-dependent reference medium

To examine the generalization capability of the neural network with respect to matrix constitutive laws, we replace the Mooney–Rivlin matrix with a neo-Hookean model while retaining rigid inclusions with perfect bonding. In the subsequent discussion of Section 4, we take ψ^h as $\psi^h = c^h(I_1^h - 3)$. Fig. 8 compares nonlinear ENM predictions with FEM results reported in Guo et al. (2014) across volume fractions of $v^i = 0.05$, 0.1, and 0.2. ENM remains stable and accurate even at large strains and high inclusion content (Fig. 8a), exhibiting a broader convergence range than FEM. These results demonstrates the adpatablility of reference medium-PGNN in this framework.

Fig. 8b plots the effective parameter c^h versus the first invariant I_1^h. Both methods predict that c^h increases with deformation, with a stronger rate of increase at higher inclusion fractions. Contrary to previous assumptions that c^h remains constant under finite deformation (Chen et al., 2019), Fig. 8b demonstrates that this assumption is approximately valid only under conditions of low volume fractions or small strains.

As we take $c^{rm} = c^h$, these results reveal that c^{rm} cannot be regarded as constant under finite deformation. Instead, its significant variation at large strains justifies the incorporation of the incremental term $\partial c^{rm}/\partial \bar{\mathbf{E}}$ in the modulus expressions (Eqs. (10) and (11)), thereby reinforcing the physical basis of the ENM framework.

To examine the advantage of ENM over the traditional reference medium approach with modulus uniform within each phase (uniform inside the matrix and within each inclusion, irrespective of the local deformation state), we consider composites with deformable inclusions. We assume that both the isotropic matrix and inclusions follow the neo-Hookean model, $\psi = c(I_1 - 3)$, with inclusion-to-matrix modulus ratio $c^i/c^m = 2$, 10, and 100, all at an inclusion volume fraction $v^i = 0.2$. Fig. 9 presents the

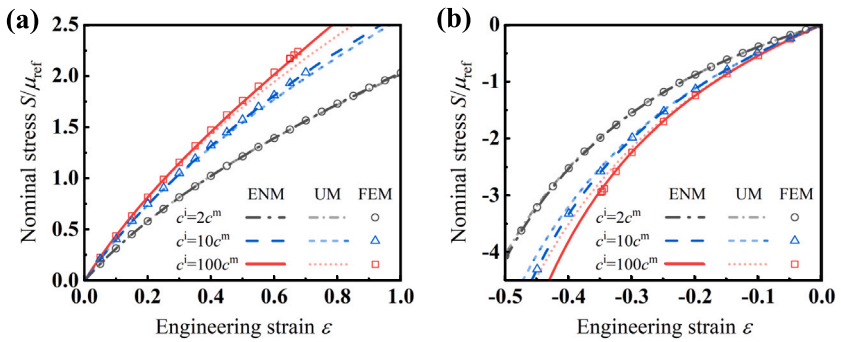

Fig. 9. Stress–strain responses under tension (a) and compression (b) predicted by ENM compared with the classical uniform-modulus reference medium method. Three cases with nonlinear inclusions having modulus ratios $c^i/c^m = 2$, 10, and 100 are examined. FEM data are from Guo et al. (2014).

stress–strain curves under tensile and compressive loading. Dark curves correspond to ENM, while light-colored curves represent the uniform-modulus (UM) approach, in which the strain within each phase is replaced by its averaged value ($\mathbf{E}^{rm} = \mathbf{E}^{\infty}$ in the reference medium and $\mathbf{E}^i = \bar{\mathbf{E}}^i$ in each inclusion). Accordingly, we set $I_1^{rm} = I_1(\mathbf{E}^{\infty})$ and $I_1^i = I_1(\bar{\mathbf{E}}^i)$ in UM, instead of the definition in Section 2.4.2. At $c^i = 2c^m$, where the inclusion and matrix moduli are similar, both methods closely match the FEM results. As the modulus contrast increases significantly, particularly at $c^i = 100c^m$, the UM method deviates significantly from FEM, whereas ENM predictions remain accurate, especially at large deformation. This improvement arises from ENM's ability to capture the strong nonlinearity induced by pronounced strain concentration around stiff inclusions.

4.3. Situations with both nonlinear inclusions and interfaces

The ENM is applicable to composites with multiple inclusion types as well as to systems where nonlinear inclusions, matrices, and complex interfaces coexist. To further assess its generality, we examine cases involving inclusion debonding (Fig. 10). The inclusion–matrix interface is modeled using the exponential cohesive zone law (Siegmund and Needleman, 1997)

$$\mathbf{t}^{int}(\Delta\mathbf{u}) = \sigma_c \exp\left(1 - \frac{|\Delta\mathbf{u}|}{\delta_c}\right)\frac{\Delta\mathbf{u}}{\delta_c}, \tag{33}$$

where the peak traction is set as $\sigma_c = 4\mu_{ref}$, δ_c is a characteristic length associated with the decohesion process, taken as $\delta_c = 0.3a$. Three composite scenarios are considered: (i) $v^i = 0.2$ and $c^i = 10c^m$; (ii) one at $v^i = 0.2$ and $c^i = 2c^m$; and (iii) a binary mixture with $v_1^i = 0.12$, $c_1^i = 10c^m$ and $v_2^i = 0.08$, $c_2^i = 10c^m$.

Calculations are carried out using both ENM and FEM, with the FEM setup following Chen et al. (2024). Fig. 10a shows the macroscopic stress–strain responses. Incorporating low-modulus inclusions lowers the overall stiffness and stress levels, while also postponing the onset of macroscopic softening. This delay arises because compliant inclusions relieve stress concentration on the surrounding matrix and interfaces, thereby reducing the driving force for debonding. As a result, a higher global strain is required before a critical fraction of the interface undergoes failure, shifting the onset of softening to later stages of deformation. Fig. 10b shows the normal stress component of the inclusions in the loading direction ($\bar{S}^i = \mathbf{e}_l \cdot \bar{\mathbf{S}}^i \cdot \mathbf{e}_l$, where $\mathbf{e}_l$ is the unit vector along the applied load), together with the debonding patterns predicted by ENM at macroscopic engineering strains of 0.36, 0.64, and 0.88. The percentages indicate the interfacial area fraction with $|\Delta\mathbf{u}| > \delta_c$, corresponding to the softening regime of the interface.

The debonding patterns exhibit distinctive morphologies, with regions undergoing larger separations initiating damage earlier and thereby accelerating further opening. As the applied strain increases, the stress contribution from inclusions and interfaces initially rises due to load transfer, but subsequently declines with progressive debonding and interfacial damage. Low-modulus inclusions smooth the evolution of damage, as deformation is accommodated primarily within the inclusions rather than the interfaces, whereas stiffer inclusions concentrate strain at the interfaces and promote earlier debonding.

Each ENM computation in Sections 4.1–4.3 is completed within 0.4 s, representing a two-order-of-magnitude improvement in computational efficiency compared to the method of Chen et al. (2024). All these calculations are performed using the same PGNNs, without retraining. This demonstrates that a single well-trained network can efficiently accommodate variations in matrix properties, interfacial conditions, inclusion volume fraction, and other factors, thereby confirming the generality of the proposed nonlinear micromechanical framework across diverse scenarios.

5. Application to plasticity

To demonstrate the broad applicability of ENM beyond hyperelasticity, we apply the method to yielding in porous plastic materials. The study assume that geometric nonlinearity is neglected, that differences among various strain and stress measures are

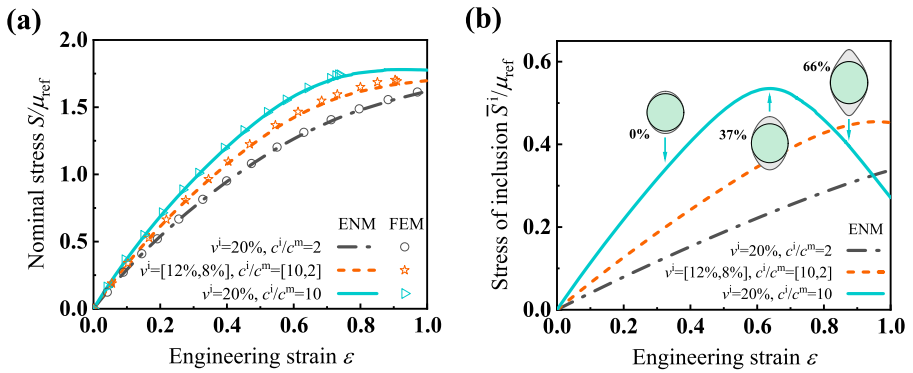

Fig. 10. Three composite cases with a total inclusion volume fraction of 0.2 are examined: (i) single-type inclusions with $c^i = 10c^m$, (ii) single-type inclusions with $c^i = 2c^m$, and (iii) a bimodal mixture with $v_1^i = 0.12$, $c_1^i = 10c^m$ and $v_2^i = 0.08$, $c_2^i = 2c^m$. In all cases, the inclusion–matrix interface follows an exponential cohesive zone law in Eq. (33). (a) Stress–strain curves computed by ENM are compared with FEM results. (b) The normal stress component of the inclusions in the loading direction. Insets, three debonding patterns at $\varepsilon = 0.36$, 0.64, and 0.88 for the case of $c^i = 10c^m$.

ignored (i.e., the total strain $\boldsymbol{\varepsilon}$ coincides with the engineering strain $\mathbf{E}$, and the Cauchy stress $\boldsymbol{\sigma}$ coincides with the first Piola–Kirchhoff stress $\mathbf{S}$).

The reference modulus μ_{ref} is identified with the yield stress σ_y of the isotropic matrix. The matrix behavior is described by the classical power-law hardening model (Tabor, 1951)

$$\varepsilon^{pl} = \begin{cases} 0, & \text{for} \quad \sigma_e < \sigma_y, \\ \dfrac{\sigma_y}{E}\left[\left(\dfrac{\sigma_e}{\sigma_y}\right)^n - 1\right], & \text{for} \quad \sigma_e \geq \sigma_y, \end{cases} \tag{34}$$

where ε^{pl} is the equivalent plastic strain, σ_e is the effective von Mises stress, E is the Young's modulus, and n denotes the hardening property. Accounting for both elastic and plastic contributions, the total strain $\boldsymbol{\varepsilon}$ is

$$\boldsymbol{\varepsilon} = \mathbf{L}^{-1} : \boldsymbol{\sigma} + \frac{3}{2}\frac{\varepsilon^{pl}}{\sigma_e}\mathbf{s}, \tag{35}$$

where $\mathbf{L}^{-1}$ is the compliance tensor, $\boldsymbol{\sigma}$ is the Cauchy stress, and $\mathbf{s} = \boldsymbol{\sigma} - \mathrm{tr}(\boldsymbol{\sigma})\mathbf{I}/3$ is the deviatoric stress. c^{rm} in this constitutive model includes σ_y/E, n, and Poisson ratio ν. Eq. (2) is accordingly reformulated as $\boldsymbol{\varepsilon} = \Psi_\sigma\left(c, \boldsymbol{\sigma}/\mu_{ref}\right)$. Since the inclusions are voids, the homogenization Eq. (4b) reduces to $\bar{\boldsymbol{\sigma}} = v^m\bar{\boldsymbol{\sigma}}^m$. The invariant relation between the reference medium displacement $\mathbf{U}^{rm}$ and traction $\mathbf{T}^{rm}$, represented by the PGNN, now reads

$$\mathbf{U}^{rm}(R) = \mathcal{Q}_\sigma^{rm}\left(c^{rm}, \mathbf{T}^{rm}(R), \frac{\boldsymbol{\sigma}^\infty}{\mu_{ref}}\right), \quad \text{for} \ R > a, \tag{36}$$

where $\boldsymbol{\sigma}^\infty$ is the far-field stress in the SIP induced by the prescribed macroscopic traction. Based on Eq. (36), we train the reference medium-PGNN, which models the mapping $\mathcal{Q}_\sigma^{rm}$, by taking the dimensionless quantities c^{rm}, $\mathbf{T}^{rm}(R)$, and $\boldsymbol{\sigma}^\infty$ as inputs, and $\mathbf{U}^{rm}(R)$ as the target output. Following a derivation parallel to Section 2.2–2.4 but in the form of stress rather than strain, the concentration tensor $\mathbf{R}^c$ in Eq. (7) is obtained as shown in Appendix D. Subsequently, the tangent modulus tensor $\mathbf{L}^h$ and the stress–strain relation is calculated.

A SIP finite element model with a plastic reference medium is constructed to generate the training data for the neural network, following the settings in Section 3.1 with two modifications: (i) the isotropic reference medium now follows the constitutive law of Eq. (35), and (ii) the far-field boundary condition is prescribed by traction loading instead of displacement control. Multiaxial loading is considered with varying stress triaxialities $\eta = \sigma_m/\sigma_e$ ($1/3 < \eta < 5$), with σ_m denoting the hydrostatic stress. Since $\mathbf{U}^{rm}$ scales linearly with σ_y/E, we fix σ_y/E to a specific value in the FEM simulations and obtain results for $\mathbf{U}^{rm}$ at other values of σ_y/E by simple rescaling. In the present study, σ_y/E is set to 1, while n varies from 5 to 20 and Poisson ratio ν ranges from 0.25 to 0.35.

The investigated porous material contains 4% voids, with the plastic matrix characterized by $\sigma_y/E = 0.004$, $n = 10$, and $\nu = 0.3$. Fig. 11a shows the learned nonlinear invariant relation, where the dimensionless first Fourier coefficients of stress in the principal directions, T_{x1}^{rm} and $T_{\rho 1}^{rm}$, serve as independent variables, while the corresponding displacement coefficients U_{x1}^{rm} and $U_{\rho 1}^{rm}$ act as dependent variables. The surface of the plastic invariant relation remains planar—indicating linear elastic behavior—over a wide low-stress regime, but bends sharply once yielding is approached. Fig. 11b compares stress–strain curves obtained by ENM and FEM at different stress triaxialities η. The stress and strain are the components of in the loading direction ($\sigma = \mathbf{e}_l \cdot \boldsymbol{\sigma} \cdot \mathbf{e}_l$ and $\varepsilon = \mathbf{e}_l \cdot \boldsymbol{\varepsilon} \cdot \mathbf{e}_l$, where $\mathbf{e}_l$ is the unit vector along the applied load) The agreement between the two methods is excellent, capturing both the onset of yielding and the subsequent nonlinear response.

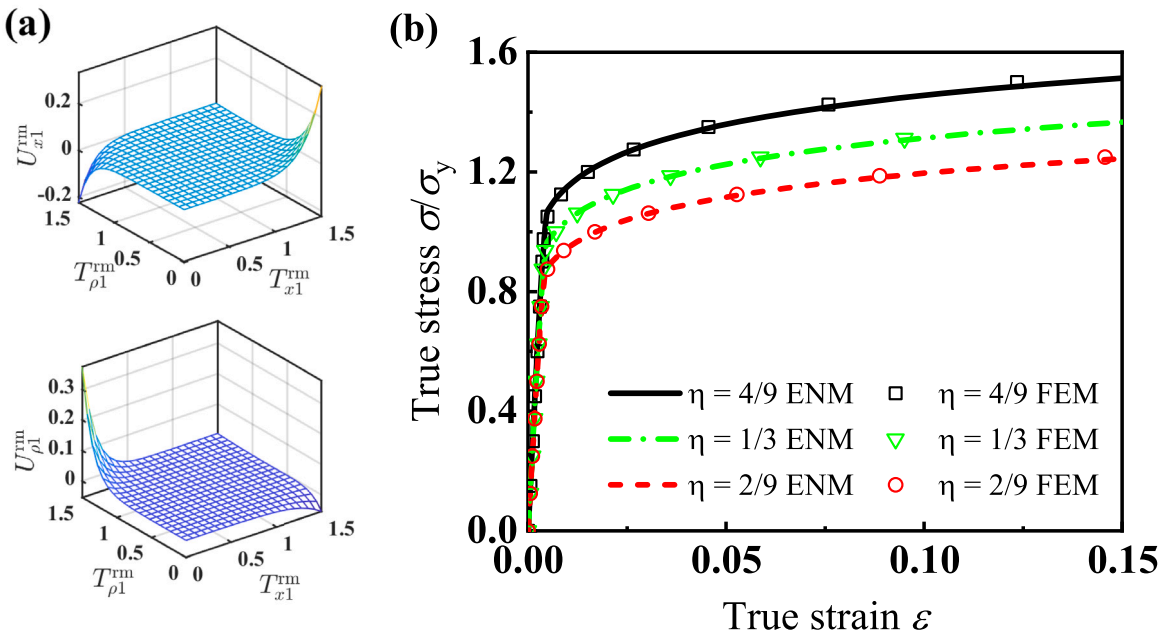

Fig. 11. (a) Learned nonlinear invariant relation of the plastic reference medium. (b) True stress–strain responses at three stress triaxialities ($\eta = 4/9$, $1/3$, and $2/9$) computed by ENM, compared with the FEM results.

6. Conclusion

This work presents a neural-network-enhanced micromechanical framework for nonlinear heterogeneous materials, in which the isotropic reference medium features a spatially non-uniform modulus that evolves with deformation. The evolution of this modulus field is optimized to capture the surrounding deformation-dependent environment. By taking advantage of invariant relations applicable to spherical surfaces of any radius and leveraging plentiful data from a single finite element simulation, the PGNNs predict the nonlinear interfacial responses of both the isotropic inclusions and the isotropic reference medium, enabling an explicit expression for the macroscopic tangent modulus and efficient evaluation of the overall stress–strain response. Moreover, the use of PGNNs eliminates the need for extensive data generation. Beyond its accuracy, the framework exhibits strong adaptability to a wide range of nonlinear constitutive behaviors and loading scenarios, offering a general and computationally efficient route for multiscale modeling of complex heterogeneous materials.

CRediT authorship contribution statement

Ce Chen: Writing – original draft, Validation, Software, Methodology, Formal analysis, Conceptualization. **Liujun Wu:** Writing – review & editing, Methodology. **Chenyang Xin:** Writing – review & editing, Software. **Wenbin Liu:** Writing – review & editing, Conceptualization. **Xin Yi:** Writing – review & editing, Methodology, Conceptualization. **Huiling Duan:** Writing – review & editing, Supervision, Project administration, Funding acquisition.

Declaration of competing interest

The authors declare that they have no known competing financial interests or personal relationships that could have appeared to influence the work reported in this paper.

Acknowledgments

H. D. acknowledges the financial support provided by the National Natural Science Foundation of China (Nos. 12588301 and 52441101).

Appendix A. Concentration tensors expressed via reference medium property variation

The strain contributions from the inclusions and interface, denoted by $\bar{\mathbf{E}}_k^{\mathrm{i}}$ and $\bar{\mathbf{E}}^{\mathrm{int}}$ in Eq. (4) can be substituted using Eqs. (8) and (9). The substitution yields the relation between $\bar{\mathbf{E}}$ and $\bar{\mathbf{E}}^{\mathrm{m}}$ as

$$\bar{\mathbf{E}} = v^{\mathrm{m}}\bar{\mathbf{E}}^{\mathrm{m}} + \sum_k v_k^{\mathrm{i}}\left[\mathcal{G}_k^{\mathrm{i}}\left(w^c\left(c^{\mathrm{m}}, c^{\mathrm{h}}\right), w^{\mathbf{E}}\left(\bar{\mathbf{E}}^{\mathrm{m}}, \bar{\mathbf{E}}\right)\right) + \mathcal{G}_k^{\mathrm{int}}\left(w^c\left(c^{\mathrm{m}}, c^{\mathrm{h}}\right), w^{\mathbf{E}}\left(\bar{\mathbf{E}}^{\mathrm{m}}, \bar{\mathbf{E}}\right)\right)\right], \tag{A.1}$$

which further gives the relation between the increments $\dot{\bar{\mathbf{E}}}$ and $\dot{\bar{\mathbf{E}}}^{\mathrm{m}}$ follows in the form

$$\mathbf{B}^{\mathrm{m}} : \dot{\bar{\mathbf{E}}}^{\mathrm{m}} = \mathbf{B}^{\mathrm{h}} : \dot{\bar{\mathbf{E}}}, \tag{A.2}$$

where $\mathbf{B}^{\mathrm{m}}$ and $\mathbf{B}^{\mathrm{h}}$ are defined as

$$\begin{cases} \mathbf{B}^{\mathrm{m}} = v^{\mathrm{m}}\mathbf{I} + \sum_k v_k^{\mathrm{i}}\left(\dfrac{\partial \mathcal{G}_k^{\mathrm{i}}}{\partial \mathbf{E}^{\infty}} + \dfrac{\partial \mathcal{G}_k^{\mathrm{int}}}{\partial \mathbf{E}^{\infty}}\right) : \dfrac{\partial w^{\mathbf{E}}}{\partial \bar{\mathbf{E}}^{\mathrm{m}}}, & \text{(A.3a)} \\ \mathbf{B}^{\mathrm{h}} = \mathbf{I} - \sum_k v_k^{\mathrm{i}}\left[\left(\dfrac{\partial \mathcal{G}_k^{\mathrm{i}}}{\partial c^{\mathrm{rm}}} + \dfrac{\partial \mathcal{G}_k^{\mathrm{int}}}{\partial c^{\mathrm{rm}}}\right)\dfrac{\partial w^c}{\partial c^{\mathrm{h}}} + \left(\dfrac{\partial \mathcal{G}_k^{\mathrm{i}}}{\partial \mathbf{E}^{\infty}} + \dfrac{\partial \mathcal{G}_k^{\mathrm{int}}}{\partial \mathbf{E}^{\infty}}\right) : \dfrac{\partial w^{\mathbf{E}}}{\partial \bar{\mathbf{E}}}\right]. & \text{(A.3b)} \end{cases}$$

By substituting $\dot{\bar{\mathbf{E}}}^{\mathrm{m}}$ with $\dot{\bar{\mathbf{E}}}$ in Eqs. (8) and (9) and organizing the equations into the forms of Eqs. (5) and (6), the concentration tensors $\mathbf{R}^{\mathrm{c}}$ and $\mathbf{W}^{\mathrm{c}}$ are obtained as

$$\begin{cases} \mathbf{R}^{\mathrm{c}} = \dfrac{\partial \mathcal{G}^{\mathrm{i}}}{\partial c^{\mathrm{rm}}}\dfrac{\partial c^{\mathrm{rm}}}{\partial \bar{\mathbf{E}}} + \dfrac{\partial \mathcal{G}^{\mathrm{i}}}{\partial \mathbf{E}^{\infty}} : \dfrac{\partial w^{\mathbf{E}}}{\partial \bar{\mathbf{E}}} + \dfrac{\partial \mathcal{G}^{\mathrm{i}}}{\partial \mathbf{E}^{\infty}} : \dfrac{\partial w^{\mathbf{E}}}{\partial \bar{\mathbf{E}}^{\mathrm{m}}} : \left(\mathbf{B}^{\mathrm{m}}\right)^{-1} : \mathbf{B}^{\mathrm{h}}, & \text{(A.4a)} \\ \mathbf{W}^{\mathrm{c}} = \dfrac{\partial \mathcal{G}^{\mathrm{int}}}{\partial c^{\mathrm{rm}}}\dfrac{\partial c^{\mathrm{rm}}}{\partial \bar{\mathbf{E}}} + \dfrac{\partial \mathcal{G}^{\mathrm{int}}}{\partial \mathbf{E}^{\infty}} : \dfrac{\partial w^{\mathbf{E}}}{\partial \bar{\mathbf{E}}} + \dfrac{\partial \mathcal{G}^{\mathrm{int}}}{\partial \mathbf{E}^{\infty}} : \dfrac{\partial w^{\mathbf{E}}}{\partial \bar{\mathbf{E}}^{\mathrm{m}}} : \left(\mathbf{B}^{\mathrm{m}}\right)^{-1} : \mathbf{B}^{\mathrm{h}}, & \text{(A.4b)} \end{cases}$$

which explicitly demonstrates the dependence on the evolution of c^{rm}.

Appendix B. Symmetry and spherical integration in three-dimensional scenarios

For distribution of displacement $\mathbf{U}(R)$ and traction $\mathbf{T}(R)$ (uniformly denoted by $\boldsymbol{\varphi}$) that are plane symmetric with respect to x-y, y-z, and z-x planes, the Fourier series approximation $\boldsymbol{\varphi}^{\mathrm{F}}$ in Eq. (26) can be simplified. Only terms with coefficients $\varphi_x^{(2p+1,2q)}$, $\varphi_y^{(2p+1,2q+1)}$, and $\varphi_z^{(2p+1,2q+1)}$ remain. Among these terms, all coefficients vanish except for $A_x = A_y = B_z = C_x = D_y = D_z = 1$. We express the components of $\boldsymbol{\varphi}^{\mathrm{F}}$ as $\varphi_\beta^{\mathrm{F}} = \{\varphi_\beta\} \cdot f^{\mathrm{F}}$, where f^{F} denotes the basis functions of the Fourier series and β represents the coordinate components x, y, or z. The least-squares method is adopted to minimize the residual defined in Eq. (27). This residual will reach stationary point with respect to the coefficients $\{\varphi_\beta\}$. The equations of this optimization process are organized to solve $\{\varphi_\beta\}$ in the form of

$$\left\{b_x\right\} = M_{\mathrm{c}} \cdot \left\{\varphi_x\right\}, \quad \left\{b_y\right\} = M_{\mathrm{s}} \cdot \left\{\varphi_y\right\}, \quad \text{and} \quad \left\{b_z\right\} = M_{\mathrm{s}} \cdot \left\{\varphi_z\right\}. \tag{B.1}$$

The arrays $\{b_\beta\}$ are calculated using numerical integration of the actual value $\boldsymbol{\varphi}$ in the physical fields as

$$\begin{cases} \left\{b_x\right\} = \displaystyle\int_0^{\frac{\pi}{2}}\int_0^{2\pi} \varphi_x \left\{\cos\left[(2q)\,\Phi\right]\cos\left[(2p+1)\,\Theta\right]\right\}\sin\Theta \mathrm{d}\Phi\mathrm{d}\Theta, & \text{(B.2a)} \\ \left\{b_y\right\} = \displaystyle\int_0^{\frac{\pi}{2}}\int_0^{2\pi} \varphi_y \left\{\cos\left[(2q+1)\,\Phi\right]\sin\left[(2p+1)\,\Theta\right]\right\}\sin\Theta \mathrm{d}\Phi\mathrm{d}\Theta, & \text{(B.2b)} \\ \left\{b_z\right\} = \displaystyle\int_0^{\frac{\pi}{2}}\int_0^{2\pi} \varphi_z \left\{\sin\left[(2q+1)\,\Phi\right]\sin\left[(2p+1)\,\Theta\right]\right\}\sin\Theta \mathrm{d}\Phi\mathrm{d}\Theta. & \text{(B.2c)} \end{cases}$$

Notes that it is a coincidence that the matrix M_{c} and M_{s} are exactly equal to the matrix M_x and M_ρ in Chen et al. (2024), respectively. The procedure above is abbreviated by the functional $\mathcal{I}^{\{b\}}$, such that $\{\varphi\} = M^{-1} \cdot \mathcal{I}^{\{b\}}(\boldsymbol{\varphi})$. Here, M refers to M_{c} or M_{s} depending on the direction of components.

Based on the Fourier series, the functional $\mathcal{A}(\boldsymbol{\varphi}^{\mathrm{F}})$ is given by

$$\mathcal{A}(\boldsymbol{\varphi}^{\mathrm{F}}) = -\sum_{p=0}^{p_{\max}} \frac{3}{(2p+3)(2p+1)(2p-1)} \begin{bmatrix} (2p+1)\,\varphi_x^{(2p+1,0)} & 0 & 0 \\ 0 & \varphi_y^{(2p+1,1)} & 0 \\ 0 & 0 & \varphi_z^{(2p+1,1)} \end{bmatrix}. \tag{B.3}$$

For the CZM interface model, $\mathbf{t}^{\mathrm{int}}$ expressed the nonlinear mapping from displacement jump to traction of every point. However, the Fourier coefficients do not follow the same nonlinear mapping as it works in linear processes. Moreover, interface models are typically defined as continuous function models in a local coordinate system. Here, we provide a tricky procedure to handle the discretization process for the derivation of interface model $\partial \mathbf{t}^{\mathrm{int}}/\partial \Delta\mathbf{u}$. The coefficients $\{\Delta U\}$ determine the approximate distribution of displacement jump, which we denoted as $\Delta u^{\mathrm{F}} = a\{\Delta U\} \cdot f^{\mathrm{F}}$. The displacement is convert from the primary coordinate β (x, y, z) to the local coordinate l (R, Θ, Φ) by metric tensor $\mathbf{g}$ with component form as $u_l^{\mathrm{F}} = g_{l\beta}u_\beta^{\mathrm{F}}$. After implementing the local interface model $\mathbf{t}^{\mathrm{F}} = \mathbf{t}_{\mathrm{local}}^{\mathrm{int}}(\Delta\mathbf{u}^{\mathrm{F}})$, restore the coordinate system to the primary coordinate α as $t_\beta^{\mathrm{F}} = g_{l\beta}^{-1}t_l^{\mathrm{F}}$. Finally, extract the Fourier coefficients

of traction with matrix M and functional $\mathcal{I}^{\{b\}}$ with the procedure of Eqs. (B.1)–(B.2). Then the discrete form of $\partial \mathbf{t}^{\text{int}}/\partial \Delta \mathbf{u}$ at local interfaces in the sense of the Fourier coefficients is derived as

$$\frac{\partial \left\{ I^{\text{int}} \right\}}{\partial \left\{ \Delta u \right\}} = \frac{\mu_{\text{ref}}}{a} \frac{\partial \left\{ T^{\text{int}} \right\}}{\partial \left\{ \Delta U \right\}} = M^{-1} \cdot \mathcal{I}^{\{b\}} \left(\mathbf{g}^{-1} \cdot \frac{\partial \mathbf{t}^{\text{int}}_{\text{local}}}{\partial \Delta \mathbf{u}} \cdot \mathbf{g} \right) \cdot f^{\text{F}}. \tag{B.4}$$

Appendix C. Tangent modulus calculation

In the computational system (Eq. (19)), the evolution of reference medium properties $\dot{c}^{\text{rm}}$ will be substituted using the following equation for the homogenized material:

$$\frac{\dot{\bar{\mathbf{S}}}}{\mu_{\text{ref}}} = \frac{\partial \Psi^{\text{h}}}{\partial \bar{\mathbf{E}}} \dot{\bar{\mathbf{E}}} + \frac{\partial \Psi^{\text{h}}}{\partial c^{\text{h}}} \left(\frac{\partial w^{c}}{\partial c^{\text{h}}} \right)^{-1} \dot{c}^{\text{rm}}. \tag{C.1}$$

By re-organizing Eqs. (20) and (21) with (C.1), and taking $\dot{\mathbf{E}}^{\infty}$, $\dot{\mathbf{U}}^{\text{rm}}_{a}$, $\dot{\mathbf{U}}^{\text{i}}_{a}$, and $\dot{c}^{\text{h}}$ as variables, we obtain

$$\mathbf{l}_{\text{r}} \begin{pmatrix} \dot{\mathbf{E}}^{\infty} \\ \dot{\mathbf{U}}^{\text{rm}}_{a} \\ \dot{\mathbf{U}}^{\text{i}}_{a} \end{pmatrix} - \frac{\partial \Psi^{\text{h}}}{\partial c^{\text{h}}} \left(\frac{\partial w^{c}}{\partial c^{\text{h}}} \right)^{-1} \dot{c}^{\text{rm}} = \mathbf{0}, \tag{C.2}$$

where the revised array $\mathbf{l}_{\text{r}}$ is denoted by

$$\mathbf{l}_{\text{r}} = \mathbf{l}_{0} - \frac{\partial \Psi^{\text{h}}}{\partial \bar{\mathbf{E}}} : \begin{pmatrix} v^{\text{m}} w^{\text{rm}} \mathbf{I} & \left(v^{\text{m}} w^{\text{i}} + v^{\text{i}} \right) \mathcal{A} & \mathbf{0} \end{pmatrix}. \tag{C.3}$$

Applying the least-squares method, the change in the non-dimensional coefficient of reference medium $\dot{c}^{\text{rm}}$ can be expressed as

$$\dot{c}^{\text{rm}} = \frac{\partial w^{c}}{\partial c^{\text{h}}} \left[\left(\frac{\partial \Psi^{\text{h}}}{\partial c^{\text{h}}} \right)^{\text{T}} : \frac{\partial \Psi^{\text{h}}}{\partial c^{\text{h}}} \right]^{-1} \left(\frac{\partial \Psi^{\text{h}}}{\partial c^{\text{h}}} \right)^{\text{T}} : \left[\mathbf{l}_{\text{r}} \begin{pmatrix} \dot{\mathbf{E}}^{\infty} \\ \dot{\mathbf{U}}^{\text{rm}}_{a} \\ \dot{\mathbf{U}}^{\text{i}}_{a} \end{pmatrix} \right], \tag{C.4}$$

where $\mathbf{l}_{\text{r}}$, defined in Eq. (C.3), is the revised array about modulus considering macroscopic property variation

Utilizing Eq. (14), we organize Eqs. (19)–(22) into the form as Eq. (5) that $\dot{\bar{\mathbf{E}}}^{\text{i}} = \mathbf{R}^{\text{c}} : \dot{\bar{\mathbf{E}}}$ and $\dot{\bar{\mathbf{S}}}^{\text{i}} = \mathbf{U}^{\text{c}} : \dot{\bar{\mathbf{S}}}$. The concentration tensors for the inclusion $\mathbf{R}^{\text{c}}$ and interface $\mathbf{W}^{\text{c}}$ can be expressed as

$$\begin{cases} \mathbf{R}^{\text{c}} = \dfrac{1}{\Delta_{\mathbf{K}_{\text{r}}}} \dfrac{a}{\mu_{\text{ref}}} \mathcal{A} \left(\dfrac{\partial \mathbf{t}^{\text{int}}}{\partial \Delta \mathbf{u}} \right)^{\text{T}} \mathbf{P}, & \text{(C.5a)} \\ \mathbf{W}^{\text{c}} = \dfrac{1}{\Delta_{\mathbf{K}_{\text{r}}}} \mathcal{A} \left(\dfrac{\partial Q^{\text{i}}}{\partial \mathbf{U}^{\text{i}}} \right)^{\text{T}} \mathbf{P}, & \text{(C.5b)} \end{cases}$$

where

$$\mathbf{P} = \frac{\partial Q^{\text{rm}}}{\partial \mathbf{E}^{\infty}} + v^{\text{m}} w^{\text{rm}} \frac{\partial Q^{\text{rm}}}{\partial c^{\text{rm}}} \frac{\partial w^{c}}{\partial c^{\text{h}}} \left[\left(\frac{\partial \Psi^{\text{h}}}{\partial c^{\text{h}}} \right)^{\text{T}} : \frac{\partial \Psi^{\text{h}}}{\partial c^{\text{h}}} \right]^{-1} \left(\frac{\partial \Psi^{\text{h}}}{\partial c^{\text{h}}} \right)^{\text{T}} : \left(\frac{\bar{\mathbf{L}}^{\text{m}}}{\mu_{\text{ref}}} - \frac{\partial \Psi^{\text{h}}}{\partial \bar{\mathbf{E}}} \right), \tag{C.6}$$

and $\Delta_{\mathbf{K}_{\text{r}}}$ is the determinant of the following array $\mathbf{K}_{\text{r}}$

$$\mathbf{K}_{\text{r}} = \mathbf{K}_{0} - \begin{pmatrix} \mathbf{0} \\ \mathbf{0} \\ \mathbf{1} \end{pmatrix} \frac{\partial Q^{\text{rm}}}{\partial c^{\text{rm}}} \frac{\partial w^{c}}{\partial c^{\text{h}}} \left[\left(\frac{\partial \Psi^{\text{h}}}{\partial c^{\text{h}}} \right)^{\text{T}} : \frac{\partial \Psi^{\text{h}}}{\partial c^{\text{h}}} \right]^{-1} \left(\frac{\partial \Psi^{\text{h}}}{\partial c^{\text{h}}} \right)^{\text{T}} : \mathbf{l}_{\text{r}}. \tag{C.7}$$

For stress interface model with no displacement jump ($\mathbf{u}^{\text{int}} = \mathbf{u}^{\text{i}}(a) = \mathbf{u}^{\text{rm}}(a)$), arrays $\mathbf{K}_{0}$ and $\mathbf{l}_{0}$ in Eq. (19) are replaced by

$$\mathbf{K}_{0} = \begin{pmatrix} v^{\text{m}} w^{\text{rm}} \mathbf{I} & \left(v^{\text{m}} w^{\text{i}} + v^{\text{i}} \right) \mathcal{A} & \mathbf{0} \\ \mathbf{0} & \mathbf{I} & -\mathbf{I} \\ -\dfrac{\partial Q^{\text{rm}}}{\partial \mathbf{E}^{\infty}} & -\dfrac{\partial Q^{\text{rm}}}{\partial \mathbf{U}^{\text{rm}}} + \dfrac{a}{\mu_{\text{ref}}} \dfrac{\partial \Delta \mathbf{t}}{\partial \mathbf{u}^{\text{int}}} & \dfrac{\partial Q^{\text{i}}}{\partial \mathbf{U}^{\text{i}}} \end{pmatrix}, \tag{C.8}$$

and

$$\mathbf{l}_{0} = \begin{pmatrix} v^{\text{m}} w^{\text{rm}} \dfrac{\bar{\mathbf{L}}^{\text{m}}}{\mu_{\text{ref}}} & v^{\text{m}} w^{\text{i}} \dfrac{\bar{\mathbf{L}}^{\text{m}}}{\mu_{\text{ref}}} : \mathcal{A} & v^{\text{i}} \dfrac{\partial Q^{\text{i}}}{\partial \mathbf{U}^{\text{i}}} : \mathcal{A} + \dfrac{a}{\mu_{\text{ref}}} \dfrac{\partial \Delta \mathbf{t}}{\partial \mathbf{u}^{\text{int}}} \end{pmatrix}, \tag{C.9}$$

where $\Delta \mathbf{t}$ and $\mathbf{u}^{\text{int}}$ are distribution of traction jump and displacement at $R = a$, respectively. Using Eqs. (25) and (C.3), the concentration tensors for the stress interface model are given by

$$\mathbf{R}^{\text{c}} = \frac{1}{\Delta_{\mathbf{K}_{\text{r}}}} \mathcal{A}(\mathbf{P}) \quad \text{and} \quad \mathbf{T}^{\text{c}} = \frac{a}{\Delta_{\mathbf{K}_{\text{r}}}} \left(\bar{\mathbf{L}}^{\text{m}} \right)^{-1} : \mathcal{A} \left(\frac{\partial \Delta \mathbf{t}}{\partial \mathbf{u}^{\text{int}}} \right)^{\text{T}} \mathbf{P}. \tag{C.10}$$

Appendix D. Plasticity implement

For the plastic problem in Section 5, some equations in Section 2 are modified. For example, the core computational system Eq. (19) are reformulated as

$$\begin{pmatrix} \dot{\bar{\boldsymbol{\varepsilon}}} \\ \mathbf{0} \\ \dfrac{\partial \mathcal{Q}_\sigma^{\mathrm{rm}}}{\partial c^{\mathrm{rm}}} \dot{c}^{\mathrm{rm}} \end{pmatrix} = \mathbf{K}_0 \begin{pmatrix} \mu_{\mathrm{ref}}^{-1} \dot{\boldsymbol{\sigma}}^{\infty} \\ \dot{\mathbf{T}}_a^{\mathrm{rm}} \\ \dot{\mathbf{U}}_a^{\mathrm{i}} \end{pmatrix} \quad \text{and} \quad \dot{\bar{\boldsymbol{\varepsilon}}} = \mathbf{l}_0 \begin{pmatrix} \mu_{\mathrm{ref}}^{-1} \dot{\boldsymbol{\sigma}}^{\infty} \\ \dot{\mathbf{T}}_a^{\mathrm{rm}} \\ \dot{\mathbf{U}}_a^{\mathrm{i}} \end{pmatrix}, \tag{D.1}$$

where $\mathbf{K}_0$ and $\mathbf{l}_0$ are defined as

$$\mathbf{K}_0 = \begin{pmatrix} v^{\mathrm{m}} w^{\mathrm{rm}} \mu_{\mathrm{ref}} \left(\bar{\mathbb{L}}^{\mathrm{m}}\right)^{-1} & v^{\mathrm{m}} w^{\mathrm{i}} \mu_{\mathrm{ref}} \left(\bar{\mathbb{L}}^{\mathrm{m}}\right)^{-1} : \mathcal{A} & v^{\mathrm{i}} \mathcal{A} \\ \mathbf{0} & \mathbf{I} & \mathbf{0} \\ -\dfrac{\partial \mathcal{Q}_\sigma^{\mathrm{rm}}}{\partial \boldsymbol{\sigma}^{\infty}} & -\dfrac{\partial \mathcal{Q}_\sigma^{\mathrm{rm}}}{\partial \mathbf{T}^{\mathrm{rm}}} & \mathbf{I} \end{pmatrix}, \tag{D.2}$$

and

$$\mathbf{l}_0 = \begin{pmatrix} v^{\mathrm{m}} w^{\mathrm{rm}} \mu_{\mathrm{ref}} \left(\bar{\mathbb{L}}^{\mathrm{m}}\right)^{-1} & v^{\mathrm{m}} w^{\mathrm{i}} \mu_{\mathrm{ref}} \left(\bar{\mathbb{L}}^{\mathrm{m}}\right)^{-1} : \mathcal{A} & v^{\mathrm{i}} \mathcal{A} \end{pmatrix}. \tag{D.3}$$

Here, w^{rm} and w^{i} represent the coefficients of $\bar{\mathbf{T}}^{\mathrm{m}} = w^{\mathrm{rm}} \mathbf{T}^{\infty} + \sum_k w_k^{\mathrm{i}} \bar{\mathbf{T}}_k^{\mathrm{i}}$, which can be calculated from Eq. (4) and similar relation as Eq. (9).

The arrays $\mathbf{l}_{\mathrm{r}}$ and $\mathbf{K}_{\mathrm{r}}$ are calculated by

$$\mathbf{l}_{\mathrm{r}} = \mathbf{l}_0 - \frac{\partial \boldsymbol{\Psi}_\sigma^{\mathrm{h}}}{\partial \bar{\mathbf{T}}} : \begin{pmatrix} v^{\mathrm{m}} w^{\mathrm{rm}} \mathbf{I} & \left(v^{\mathrm{m}} w^{\mathrm{i}} + v^{\mathrm{i}}\right) \mathcal{A} & \mathbf{0} \end{pmatrix}, \tag{D.4}$$

and

$$\mathbf{K}_{\mathrm{r}} = \mathbf{K}_0 - \begin{pmatrix} \mathbf{0} \\ \mathbf{0} \\ \mathbf{1} \end{pmatrix} \frac{\partial \mathcal{Q}_\sigma^{\mathrm{rm}}}{\partial c^{\mathrm{rm}}} \frac{\partial w^c}{\partial c^{\mathrm{h}}} \left[\left(\frac{\partial \boldsymbol{\Psi}_\sigma^{\mathrm{h}}}{\partial c^{\mathrm{h}}} \right)^{\mathrm{T}} : \frac{\partial \boldsymbol{\Psi}_\sigma^{\mathrm{h}}}{\partial c^{\mathrm{h}}} \right]^{-1} \left(\frac{\partial \boldsymbol{\Psi}_\sigma^{\mathrm{h}}}{\partial c^{\mathrm{h}}} \right)^{\mathrm{T}} : \mathbf{l}_{\mathrm{r}}. \tag{D.5}$$

Similar to Eq. (3), the mapping $\boldsymbol{\Psi}_\sigma^{\mathrm{h}}$ is defined as $\bar{\boldsymbol{\varepsilon}} = \boldsymbol{\Psi}_\sigma^{\mathrm{h}} \left(c^{\mathrm{h}}, \bar{\boldsymbol{\sigma}} / \mu_{\mathrm{ref}}\right)$ with varying c^{h}.

In Eq. (7), the concentration tensor $\mathbf{W}^{\mathrm{c}}$ vanishes since there is no interface. The concentration tensor $\mathbf{R}^{\mathrm{c}}$ is calculated by $\mathbf{R}^{\mathrm{c}} = \mathcal{A}(\mathbf{P}) / \Delta_{\mathbf{K}_{\mathrm{r}}}$, where

$$\mathbf{P} = \frac{\partial \mathcal{Q}_\sigma^{\mathrm{rm}}}{\partial \boldsymbol{\sigma}^{\infty}} + v^{\mathrm{m}} w^{\mathrm{rm}} \frac{\partial \mathcal{Q}_\sigma^{\mathrm{rm}}}{\partial c^{\mathrm{rm}}} \frac{\partial w^c}{\partial c^{\mathrm{h}}} \left[\left(\frac{\partial \boldsymbol{\Psi}_\sigma^{\mathrm{h}}}{\partial c^{\mathrm{h}}} \right)^{\mathrm{T}} : \frac{\partial \boldsymbol{\Psi}_\sigma^{\mathrm{h}}}{\partial c^{\mathrm{h}}} \right]^{-1} \left(\frac{\partial \boldsymbol{\Psi}_\sigma^{\mathrm{h}}}{\partial c^{\mathrm{h}}} \right)^{\mathrm{T}} : \left[\mu_{\mathrm{ref}} \left(\bar{\mathbb{L}}^{\mathrm{m}}\right)^{-1} - \frac{\partial \boldsymbol{\Psi}_\sigma^{\mathrm{h}}}{\partial \bar{\mathbf{T}}} \right]. \tag{D.6}$$

Appendix E. Supplementary data

Supplementary material related to this article can be found online at https://doi.org/10.1016/j.jmps.2025.106426.

Data availability

No data was used for the research described in the article.

References

Avazmohammadi, R., Ponte Castañeda, P., 2013. Tangent second-order estimates for the large-strain, macroscopic response of particle-reinforced elastomers. J. Elasticity 112, 139–183.

Benaimeche, M.A., Yvonnet, J., Bary, B., He, Q., 2022. A k-means clustering machine learning-based multiscale method for anelastic heterogeneous structures with internal variables. Internat. J. Numer. Methods Engrg. 123, 2012–2041.

Benveniste, Y., Miloh, T., 2001. Imperfect soft and stiff interfaces in two-dimensional elasticity. Mech. Mater. 33, 309–323.

Brassart, L., Inglis, H.M., Delannay, L., Doghri, I., Geubelle, P.H., 2009. An extended Mori–Tanaka homogenization scheme for finite strain modeling of debonding in particle-reinforced elastomers. Comput. Mater. Sci. 45, 611–616.

Buckingham, E., 1914. On physically similar systems; illustrations of the use of dimensional equations. Phys. Rev. 4, 345–376.

Chen, C., Wu, L., Fu, J., Xin, C., Liu, W., Duan, H., 2024. A micromechanical scheme with nonlinear concentration functions by physics-guided neural network. J. Mech. Phys. Solids 188, 105681.

Chen, Y., Xin, L., Liu, Y., Guo, Z., Dong, L., Zhong, Z., 2019. A viscoelastic model for particle-reinforced composites in finite deformations. Appl. Math. Model. 72, 499–512.

Christensen, R.M., 1990. A critical evaluation for a class of micro-mechanics models. J. Mech. Phys. Solids 38, 379–404.

Christensen, R.M., Lo, K.H., 1979. Solutions for effective shear properties in three phase sphere and cylinder models. J. Mech. Phys. Solids 27, 315–330.

Dingreville, R., Qu, J., Cherkaoui, M., 2005. Surface free energy and its effect on the elastic behavior of nano-sized particles, wires and films. J. Mech. Phys. Solids 53, 1827–1854.

Duan, H., Karihaloo, B.L., Wang, J., Yi, X., 2006. Effective conductivities of heterogeneous media containing multiple inclusions with various spatial distributions. Phys. Rev. B 73, 174203.

Duan, H., Wang, J., Huang, Z., Karihaloo, B.L., 2005. Size-dependent effective elastic constants of solids containing nano-inhomogeneities with interface stress. J. Mech. Phys. Solids 53, 1574–1596.
Eshelby, J.D., 1957. The determination of the elastic field of an ellipsoidal inclusion, and related problems. Proc. R. Soc. Lond. A 241, 376–396.
Firooz, S., Chatzigeorgiou, G., Meraghni, F., Javili, A., 2019. Homogenization accounting for size effects in particulate composites due to general interfaces. Mech. Mater. 139, 103204.
Frankel, A., Jones, R., Swiler, L., 2020. Tensor basis gaussian process models of hyperelastic materials. J. Mach. Learn. Model. Comput. 1, 1–17.
Gentieu, T., Catapano, A., Jumel, J., Broughton, J., 2019. A mean-field homogenisation scheme with CZM-based interfaces describing progressive inclusions debonding. Compos. Struct. 229, 111398.
Gholami, K., Ege, F., Barzegar, R., 2023. Prediction of composite mechanical properties: Integration of deep neural network methods and finite element analysis. J. Compos. Sci. 7, 54.
Govindjee, S., Simo, J., 1991. A micro-mechanically based continuum damage model for carbon black-filled rubbers incorporating Mullins' effect. J. Mech. Phys. Solids 39, 87–112.
Guo, Z., Shi, X., Chen, Y., Chen, H., Peng, X., Harrison, P., 2014. Mechanical modeling of incompressible particle-reinforced neo-Hookean composites based on numerical homogenization. Mech. Mater. 70, 1–17.
Hagan, M.T., Menhaj, M.B., 1994. Training feedforward networks with the Marquardt algorithm. IEEE Trans. Neural Netw. 5, 989–993.
Hasan, T., Capolungo, L., Zikry, M., 2023. How can machine learning be used for accurate representations and predictions of fracture nucleation in zirconium alloys with hydride populations? APL Mater. 11, 071111.
Heitbreder, T., Kurzeja, P., Mosler, J., 2021. On general imperfect interfaces with spatially non-constant displacement jumps. Int. J. Solids Struct. 232, 111068.
Hervé, E., Zaoui, A., 1995. Elastic behaviour of multiply coated fibre-reinforced composites. Internat. J. Engrg. Sci. 33, 1419–1433.
Hervé-Luanco, E., 2020. Elastic behaviour of multiply coated fibre-reinforced composites: Simplification of the (n+1)-phase model and extension to imperfect interfaces. Int. J. Solids Struct. 196, 10–25.
Hill, R., 1965. A self-consistent mechanics of composite materials. J. Mech. Phys. Solids 13, 213–222.
Hill, R., 1972. On constitutive macro-variables for heterogeneous solids at finite strain. Proc. R. Soc. Lond. A 326, 131–147.
Holzapfel, G.A., 2000. Nonlinear Solid Mechanics: A Continuum Approach for Engineering. John Wiley & Sons, Chichester, UK.
Huang, M., Du, Z., Liu, C., Zheng, Y., Cui, T., Mei, Y., Li, X., Zhang, X., Guo, X., 2022. Problem-independent machine learning (PIML)-based topology optimization—A universal approach. Extrem. Mech. Lett. 56, 101887.
Inglis, H., Geubelle, P., Matouš, K., Tan, H., Huang, Y., 2007. Cohesive modeling of dewetting in particulate composites: micromechanics vs. multiscale finite element analysis. Mech. Mater. 39, 580–595.
Le, B., Yvonnet, J., He, Q.-C., 2015. Computational homogenization of nonlinear elastic materials using neural networks. Internat. J. Numer. Methods Engrg. 104, 1061–1084.
Linka, K., Hillgärtner, M., Abdolazizi, K.P., Aydin, R.C., Itskov, M., Cyron, C.J., 2021. Constitutive artificial neural networks: A fast and general approach to predictive data-driven constitutive modeling by deep learning. J. Comput. Phys. 429, 110010.
Logarzo, H.J., Capuano, G., Rimoli, J.J., 2021. Smart constitutive laws: Inelastic homogenization through machine learning. Comput. Methods Appl. Mech. Engrg. 373, 113482.
Lu, X., Yvonnet, J., Papadopoulos, L., Kalogeris, I., Papadopoulos, V., 2021. A stochastic FE^2 data-driven method for nonlinear multiscale modeling. Materials 14, 2875.
Mori, T., Tanaka, K., 1973. Average stress in matrix and average elastic energy of materials with misfitting inclusions. Acta Metall. 21, 571–574.
Mullins, L., Tobin, N., 1965. Stress softening in rubber vulcanizates. Part I. Use of a strain amplification factor to describe the elastic behavior of filler-reinforced vulcanized rubber. J. Appl. Polym. Sci. 9, 2993–3009.
Ponte Castañeda, P., 2002. Second-order homogenization estimates for nonlinear composites incorporating field fluctuations: I—theory. J. Mech. Phys. Solids 50, 737–757.
Raissi, M., Perdikaris, P., Karniadakis, G.E., 2019. Physics-informed neural networks: A deep learning framework for solving forward and inverse problems involving nonlinear partial differential equations. J. Comput. Phys. 378, 686–707.
Rao, Y., Qu, J., Marinis, T., Wong, C., 2000. A precise numerical prediction of effective dielectric constant for polymer-ceramic composite based on effective-medium theory. IEEE Trans. Compon. Packag. Technol. 23, 680–683.
Rivlin, R.S., Saunders, D., 1951. Large elastic deformations of isotropic materials VII. Experiments on the deformation of rubber. Philos. Trans. R. Soc. A 243, 251–288.
Sabar, H., Berveiller, M., Favier, V., Berbenni, S., 2002. A new class of micro-macro models for elastic–viscoplastic heterogeneous materials. Int. J. Solids Struct. 39, 3257–3276.
Shampine, L.F., Reichelt, M.W., 1997. The MATLAB ODE suite. SIAM J. Sci. Comput. 18, 1–22.
Shi, Y., Liu, R., Wong, C., Ye, C., Lv, J., 2024. Prediction of tensile behavior of compression therapeutic biomedical materials by mesoscale laid-in loop model. Polymer 302, 127094.
Siegmund, T., Needleman, A., 1997. A numerical study of dynamic crack growth in elastic-viscoplastic solids. Int. J. Solids Struct. 34, 769–787.
Spannraft, L., Steinmann, P., Mergheim, J., 2023. A generalized anisotropic damage interface model for finite strains. J. Mech. Phys. Solids 174, 105255.
Spring, D.W., Paulino, G.H., 2015. Computational homogenization of the debonding of particle reinforced composites: The role of interphases in interfaces. Comput. Mater. Sci. 109, 209–224.
Tabor, D., 1951. The Hardness of Metals. Oxford University Press, Oxford, UK.
Tan, H., Liu, C., Huang, Y., Geubelle, P.H., 2005. The cohesive law for the particle/matrix interfaces in high explosives. J. Mech. Phys. Solids 53, 1892–1917.
Treloar, L., 1943. The elasticity of a network of long-chain molecules—II. Trans. Faraday Soc. 39, 241–246.
Wang, J., Cao, P., Wang, X., 2023. Review of the mechanical properties and numerical simulation of composite solid propellants. Materials 16, 6875.
Wu, L., Fu, J., Sui, H., Wang, X., Tao, B., Lv, P., Chen, M., Yuan, Z., Duan, H., 2023. A data-driven yield criterion for porous ductile single crystals containing spherical voids via physics-informed neural networks. Proc. R. Soc. A 479, 20230433.
Xiao, X., Song, D., Xue, J., Chu, H., Duan, H., 2015. A self-consistent plasticity theory for modeling the thermo-mechanical properties of irradiated FCC metallic polycrystals. J. Mech. Phys. Solids 78, 1–16.